IRAQI JOURNAL OF APPLIED PHYSICS LETTERS

The Iraqi Journal of Applied Physics Letters (IJAPLett) is a peer reviewed journal of high quality devoted to the publication of original research letters from applied physics and their broad range of applications. IJAPLett publishes quality original research letters in physics and its applications in the broadest sense. It is intended that the journal may act as an interdisciplinary forum for physics and its applications. Innovative applications and material that brings together diverse areas of physics are particularly welcome. IJAPLett aims to disseminate knowledge; provide a learned reference in the field; and establish channels of communication between academic and research experts, policy makers and executives in industry, commerce and investment institutions. IJAPLett is a quarterly specialized periodical dedicated to publishing original letters in: Alternative & Renewable Energy, Applied Mechanics & Thermodynamics, Applied Optics & Optical Design, Biophysics & Bioengineering, Cryptography & Applications, Electromagnetic Fields, Electronic Materials & Devices, Energy Generation & Conversion, Fluids Physics & Mechanics, Imaging, Microscopy & Spectroscopy, Laser Physics & Applications, Magnetism & Applications, Instrumentation, Measurements & Metrology, Nanostructures & Applications, Nonlinear & Ultrafast Optics, Nuclear Physics & Engineering, Optical Communications & Systems, Optoelectronics Devices & Applications, Organic Materials, Devices & Applications, Physical Chemistry & Biochemistry, Plasma, Discharge Physics & Applications, Quantum Physics & Spectroscopy, RF & Digital Communications, Semiconductors & Devices, Simulation & Modeling Research, Solar Energy & Devices, Solid State Physics & Applications, Structure & Properties of Matter, Superconductivity & Related Devices, Surfaces, Interfaces & Films, Thin Films & Applications, and Vacuum Science & Technology.

ISSN (Print)
1999-656X
ISSN (Online)
2958-6488

EDITORIAL BOARD

Editorial Office:
P. O. Box 88052, Baghdad 12631, IRAQ
Website: www.iraqiphysicsjournal.com
Emails: editor@iraqiphysicsjournal.com, editor_ijap@yahoo.co.uk, ijaplett.editor@gmail.com

ADVISORY BOARD

SPONSORED AND PUBLISHED BY
AMERICAN QUALITY FOR SCIENTIFIC PUBLISHING INC.
1479 South De Gaulle Ct, Aurora, CO 80018, United States

IRAQI JOURNAL OF APPLIED PHYSICS LETTERS

ISSN (Print): 1999-656X, ISSN (Online): 2958-6488

INSTRUCTIONS TO AUTHORS

CONTRIBUTIONS

Contributions to be published in this journal should be original research works, i.e., those not already published or submitted for publication elsewhere, individual papers or letters to editor.
Manuscripts should be submitted to the editor at the mailing address:

Iraqi Journal of Applied Physics Letters, Editorial Board, P. O. Box 88052, Baghdad 12631, IRAQ
Website: www.iraqiphysicsjournal.com
Email: editor@iraqiphysicsjournal.com, editor_ijap@yahoo.co.uk, ijaplett.editor@gmail.com

MANUSCRIPTS

Two hard copies with soft Word copy on a CD or DVD should be submitted to Editor in the following configuration:

- **One-column** Double-spaced one-side A4 size with 2.5 cm margins of all sides
- Times New Roman font (16pt bold for title, 14pt bold for names, 12pt bold for headings, 12pt regular for text)
- Manuscripts presented in English only are accepted.
- English abstract not exceed 100 words
- 4 keywords (at least) should be maintained on (PACS preferred)
- Author(s) should express all quantities in SI units
- Equations should be written in equation form (*italic* and symbolic) NOT in plain text
- Tables and Figures should be separated from text and placed in new pages after the references
- Charts should be indicated by the software used for generating them (e.g., Excel, MATLAB, Grapher, etc.)
- Figures and diagrams can be submitted in original colored forms for assessment and they will be returned to authors after provide printable copies
- Only original or high-resolution scanner photos are accepted
- For electronic submission, articles should be formatted with MS-Word software.

AUTHOR NAMES AND AFFILIATIONS

It is IJAPLett policy that all those who have participated significantly in the technical aspects of a paper be recognized as co-authors or cited in the acknowledgments. In the case of a paper with more than one author, correspondence concerning the paper will be sent to the first author unless staff is advised otherwise.
Author name should consist of first name, middle initial, last name. The author affiliation should consist of the following, as applicable, in the order noted:
- Company or college (with department name or company division), Postal address, City, Governorate or State, zip code, Country name, contacting telephone number, and e-mail

REFERENCES

The references should be brought at the end of the article, and numbered in the order of their appearance in the paper. The reference list should be cited in accordance with the following examples:
[1] X. Ning, R. Benford and M.R. Lovell, "On the Sliding Friction Characteristics of Unidirectional Continuous FRP Composites", *J. Tribol. Func. Mater.*, 124(1) (2002) 5-13.
[2] M. Barnes, "Stresses in Solenoids", *J. Appl. Phys.*, 48(5) (2001) 2000–2008.
[3] J. Jones, **"Contact Mechanics"**, Cambridge University Press (Cambridge, UK) (2000), Ch.6, p.56.
[4] Y. Lee, S.A. Korpela and R. Horne, "Structure of Multi-Cellular Natural Convection in a Tall Vertical Annulus", Proceedings of 7th International Heat Transfer Conference, U. Grigul et al., eds., Hemisphere (Washington DC), 2 (1982) 221–226.
[5] M. Hashish, "Waterjet Technology Development", High Pressure Technology, PVP-Vol. 406 (2000) 135-140.
[6] D.W. Watson, "Thermodynamic Analysis", ASME Paper No. 97-GT-288 (1997).
[7] C.Y. Tung, "Evaporative Heat Transfer in the Contact Line of a Mixture", Ph.D. thesis, Rensselaer Polytechnic Institute, Troy, NY (1982).

PROOFS

Authors will receive proofs of papers and are requested to return one corrected copy as a WORD file on a compact disc (CD) or by email. New materials inserted in the original text without Editor's permission may cause rejection of paper unless the handling editor is informed.

COPYRIGHT FORM

Author(s) will be asked to sign the IJAPLett Copyright Form and hence transfer copyrights of the article to the Journal soon after acceptance of it. This will ensure the widest possible dissemination of information.

OFFPRINTS

Authors will receive electronic offprint free of charge and any additional reprints can be ordered.

SUBSCRIPTION AND ORDERS

Annual fees (4 issues per year) of subscription are:
50 US$ for individuals inside Iraq; **200** US$ for institutions inside Iraq;
100 US$ for individuals abroad; **300** US$ for institutions abroad.

Characteristics of Electrochemical Biosensor for Alcohol Determination in Blood Samples

Fuad K. Hussain, Majid H. Radi

Department of Physics, College of Science, Al-Qadesia University, Dewania, IRAQ

Abstract

In the current work we present a smartphone-based µPotentiostat which combines a novel circuital technique for sensor readout digitalization with a reusable lab-on-a-chip concept. Biosensing is enabled by in situ electrodeposition of a calcium alginate hydrogel containing horseradish peroxidase (HPR) and alcohol oxidase (AO_x) for selective ethanol detection. Alginate membrane electrodeposition has been here optimized for rapid generation and to retain the cellular fraction, thus allowing the measurement in whole blood samples. The µPotentiostat features a sensitivity of 36 nA/g.L^{-1} to ethanol concentration in blood in the 0–1.25 g.L^{-1} range, with a limit of quantification of 4.5 nA, which is a suitable response for discerning the legal, illegal, severely illegal thresholds in a 40 µL sample of blood.

Keywords: Biosensors; Electrochemical sensors; Alcohol sensors; Biomedical applications
Received: 17 May 2023; **Revised:** 11 June 2023; **Accepted:** 18 June 2023; **Published:** 1 September 2023

1. Introduction

The degree of ethanol intoxication of a person is assessed in a number of circumstances including traffic police checkpoints, emergency departments or emergency quick responses [1,2] and is quantified by blood alcohol concentration (BAC) [3]. Currently, hand-held breath analyzers (commonly referred to braethalyzers) are employed either for law enforcement in traffic security or for clinical trial. These devices sample patients' breath alcohol concentration (BrAC) in a rapid and non-invasive way and rely on an established BrAC/BAC ratio (BBR) to finally estimate patients' BAC [4,5]. Despite the versatility of these devices, their reliability in critical cases such as emergency situations is undermined by: (i) BBR inter-/intra-individual variability, (ii) respiratory impairment or lack of patient collaboration and (iii) presence of residual mouth alcohol. BBR values vary a lot among different countries, depending on the respective legal framework for traffic security and ranging from a 2000 to 2400 [6-8], giving rise to a fervid scientific debate [10-12]. Subject will and/or capacity to sustaining a constant breath flow through the instrument is another issue that can only be addressed by the most sophisticated and expensive models of breathalyzers. Finally test results can be false positive due to the presence of alcohol in the mouth, but not absorbed in the bloodstream: use of mouth rinses or even endogenous fermentation in human guts are possible causes of that [13].

Here, we present a BAC measurement device employing the recently published transducer structures based on electrodeposited alginate membranes [14,15] in combination with an original circuit architecture enabling the integration of complex functions over readout signals using very few discrete components.

2. Experimental Part

Alginic acid sodium salt, $CaCl_2$ (≥93 %), 2-(N-morpholino)ethanesulfonic acid hydrate (MES hydrate, ≥99 %), NaOH (≥98 %), KOH (≥86 %), 3,3′,5,5′-Tetramethylbenzidine (TMB, ≥98 %), NaCl (ACS reagent, ≥99 %), H_2O_2 (30% in H_2O), HRP (Type VI-A, essentially salt-free lyophilized powder, 250-330 units mg^{-1}) and AOx from *Pichia pastoris* (buffered aqueous

solution, 1200 units ml^{-1}) were purchased from Sigma-Aldrich. $CaCO_3$ (≥98.5 %), $K_3[Fe(CN)_6]$ (ACS reagent, ≥99 %), dimethyl sulphoxide (DMSO, 99.5 %), Na_2HPO_4 (ACS reagent, ≥99 %) and ethanol absolute (≥99.5 %) were purchased from Panreac. KCl (≥99 %) and KH_2PO4 (ACS reagent, ≥99.5 %) were purchased from Fluka.

As the recognition part of the biosensor, a reversible electrodepositable calcium alginate hydrogel was used for the enzymes retention, following a previously reported protocol [14]. The measure cycle consists in three main steps: hydrogel electrodeposition, amperometric detection and hydrogel removal. Briefly, for the electrodeposition, an alginic acid sodium salt was dissolved in warm water with magnetic stirring and then mixed with $CaCO_3$ and the enzymes. Subsequently, it was injected into the reaction chamber of the device through the channel. In presence of $CaCO_3$ particles, the application of an anodizing potential (1.5 V vs. RE) promotes water oxidation into O_2 and protons. These protons react with the $CaCO_3$ particles, promoting their dissociation into Ca^{2+} cations and HCO_3^-. Finally, the Ca^{2+} cations complete the cross-link reaction among the alginic acid monomers and a gel is formed, attached to the anodized electrode (WE) [16]. After the electrodeposition, the chamber is washed with deionized water to remove the excess of precursor and leave only the recently built hydrogel. For the measurement, the sample was introduced in the chamber and a constant potential of 0 V (vs. Pt RE) was applied between the WE and the RE, while the current was measured between the WE and the CE. The registered current is related to the initial amount of ethanol in the medium due to the following cascade reaction [17]:

$$CH_3CH_2O + O_2 \xrightarrow{\text{alcohol oxidase}} CH_3CHO + H_2O_2$$

$$H_2O_2 + TMB_{red} \xrightarrow{\text{peroxidase}} H_2O + TMB_{ox}$$

where the ethanol is first oxidized by the AOx into acetaldehyde and hydrogen peroxide (1) and this is used by the HRP to oxide the TMB (2) which is present as a mediator. Finally the oxidized TMB is reduced at the WE at the applied potential. Once the measurement is finished, the chamber and the channel were cleaned using PBS. The phosphate acts as a chelating agent, trapping Ca^{2+} and disaggregating the gel rapidly. The process can then start from the beginning in a second analysis using the same device and only regenerating the membrane.

3. Results and Discussion

The µPotentiostat has been characterized through cyclic voltammetry experiments of the $Fe^{III}(CN)_6^{3-}/Fe^{II}(CN)_64^-$ couple. Figure 3 shows the results for a 1 mM Ferri-Ferro in 150 mM KCl at different scan rates compared to the benchtop instrument. For this experiment the DAC resistor was fixed to be 330 kohm, in order to provide a nominal current full-scale of 5 µA (both positive and negative). Data was extracted recording the digital signal *qdsm* sampled at 2.5 kS/s. At this point, since *qdsm* contains the high frequency quantization noise, filtering is needed to correctly reconstruct the WE current waveform: ideally an analog bessel filter should be employed to preserve the group delay of the signal, in practice a digital equivalent derived from the analog model through a bilinear transform is sufficient since the bandwidth of interest is much lower than the sampling frequency, this way the high frequency noise evident is largely suppressed. The tuning parameter of the filter must be adjusted to accordingly since the bandwidth of interests scale proportionally to the scan-rate. It is worth noting that an excessive filtering should be carefully chosen in order to avoid filtering frequency component of the signal of interest. For the third-order digital Bessel filter used here, the critical frequency at phase response midpoint has been set to 0.67 Hz, 8.33 Hz, 20.83 Hz for the scan-rates of 2 mV/s, 10 mV/s and 25 mV/s, respectively.

The comparison between the µPotentiostat versus the bench-top cyclic voltammetries are evident in Fig. (1a,b), where it can be seen that some high frequency noise is still visible in our system. A smoother characteristic can be obtained, without bandwidth impairment, by averaging several cycles.

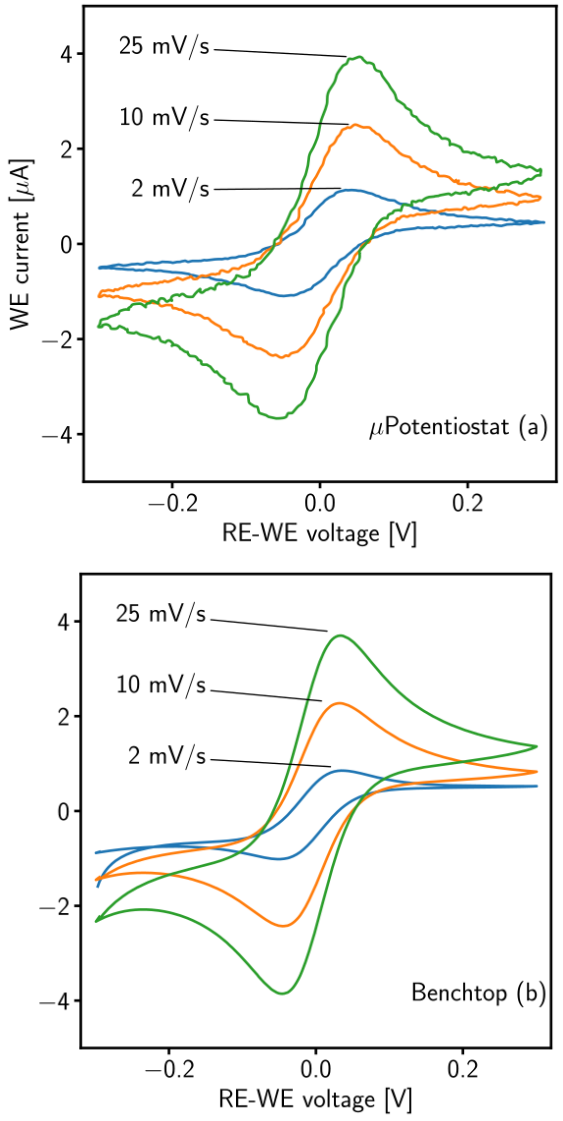

Fig. (1) Cyclic voltammetries of 1 mM Ferri-Ferro in 150 mM KCl at different scan rates: (a) µPotentiostat and (b) bench-top setup

4. Conclusion

In conclusion, The system reports on glucose and hydrogen peroxide concentrations, conductivity and ORP as a way to monitor cell metabolism. In addition to the latter, electrochemical analysis is completed with high-resolution imaging by confocal microscopy after labelling with fluorescent dyes. Induction of oxidative stress by hydrogen peroxide produces a dose-dependent reduction of glucose consumption and a proportional increase of DHE emission.

References

[1] A.G.A. Aggidis, J.D. Newman and G.A. Aggidis, "Investigating pipeline and state of the art blood glucose biosensors to formulate next steps", *Biosens. Bioelectron.*, 74 (2015) 243–262.

[2] D. Zhang and Q. Liu, "Biosensors and bioelectronics on smartphone for portable biochemical detection", *Biosens. Bioelectron.*, 75 (2016) 273–284.

[3] A.C. Sun et al., "An efficient power harvesting mobile phone-based electrochemical biosensor for point-of-care health monitoring", *Sensors Actuators B Chem.*, 235 (2016) 126–135.

[4] Y. Fan et al., "A wireless point-of-care testing system for the detection of neuron-specific enolase with microfluidic paper-based analytical devices", *Biosens. Bioelectron.*, 95 (2017) 60–66.

[5] A.F.D. Cruz, N. Norena and S.B. Ajeet Kaushik, "A low-cost miniaturized potentiostat for point-of-care diagnosis", *Biosens. Bioelectron.*, 62 (2014) 249–254.

[6] X. Wang et al., "White blood cell counting on smartphone paper electrochemical sensor", *Biosens. Bioelectron.*, 90 (2017) 549–557.

[7] C. Loncaric et al., "A USB-based electrochemical biosensor prototype for point-of-care diagnosis", *Sensors Actuators B Chem.*, 161 (2012) 908–913.

[8] D. Ji et al., "Smartphone-based cyclic voltammetry system with graphene modified screen printed electrodes for glucose detection", *Biosens. Bioelectron.*, 98 (2017) 449–456.

[9] X. Wang et al., "Audio jack based miniaturized mobile phone electrochemical sensing platform", *Sensors Actuators B Chem.*, 209 (2015) 677–685.

[10] E. Aronoff-Spencer et al., "Detection of Hepatitis C core antibody by dual-affinity yeast chimera and smartphone-based electrochemical sensing", *Biosens. Bioelectron.*, 86 (2016) 690–696.

[11] S. Sutula et al., "A 25-µW All-MOS Potentiostatic Delta-Sigma ADC for Smart Electrochemical Sensors", *IEEE Trans. Circuits Syst. I Regul. Pap.*, 61 (2014) 671–679.

[12] I. Ramfosa et al., "A compact hybrid-multiplexed potentiostat for real-time electrochemical biosensing applications", *Biosens. Bioelectron.*, 47 (2013) 482–489.

[13] A. Roda et al., "Smartphone-based biosensors: A critical review and perspectives", *TrAC Trends Anal. Chem.*, 79 (2013) 317–325.
[14] P.B. Lillehoj et al., "Rapid electrochemical detection on a mobile phone", *Lab Chip*, 13 (2013) 2950–2955.
[15] D. Quesada-González and A. Merkoçi, "Mobile phone-based biosensing: An emerging "diagnostic and communication" technology", *Biosens. Bioelectron.*, 92 (2017) 549–562.
[16] A. Márquez et al., "Electrodepositable alginate membranes for enzymatic sensors: An amperometric glucose biosensor for whole blood analysis", *Biosens. Bioelectron.*, 97 (2017) 136–142.
[17] J. Orozco et al., "Characterization of ultramicroelectrode arrays combining electrochemical techniques and optical microscopy imaging", *Electrochim. Acta*, 53 (2007) 729–736.

Characterization of Silicon Nanowires Fabricated by Metal-Assisted Chemical Etching

Tsang Pui Yuen

Department of Physics and Materials Science, University of Hong Kong, Hong Kong, CHINA

Abstract

In this work, the synthesis of silicon nanowires arrays by metal-assisted chemical etching and their structural characteristics have been presented. The Si substrates were cut into small square pieces and immersed in different concentrations of H_2O_2 and HF solutions. After that, a gold coating was formed through the reaction with $HAuCl_4$ and HF solution. After the etching process, the six different silicon nanowires reacting with different concentrations of etchants were took to several characterizing microscopes to study their surface morphology. These properties can be obtained by the microscopes mentioned after reacting with the chemical etchants HF and H_2SO_4.

Keywords: Silicon nanowires; Porous silicon; Chemical etching; Structural characterization
Received: 25 March 2023; **Revised:** 20 June 2023; **Accepted:** 27 June 2023; **Published:** 1 September 2023

1. Introduction

More and more efforts have been put to nanotechnology because when materials come to nano size, there will be some unique properties of the materials. The word "nano" is used to describe materials with the dimension of 10^{-9} m, normally from 1 to 100 nm [1]. There is a great difference in physical and chemical properties between bulk materials and nanomaterials at this nanometer scale due to the quantum size effect, surface-to-volume ratio and boundary effect of the basic structure [2]. For instance, there is continuous reduction in the diameter of silicon nanowires from about 7 down to about 1.3 nm causing energy bandgap of silicon from 1.1 up to 3.5 eV increases gradually [3,4]. Theoretically, if one of the dimensions (e.g. along x-axis) is reduced to the range of 1 to 100 nm, the material becomes two-dimensional (2D) nanostructure, as well as in the form of ultrathin films [5]. On the other hand, if another dimension (e.g., y-and z-axis) is also reduced to nanometer scale, the materials will become one-dimensional (1D) nanostructure in from of wires, ribbons, rods, tubes [6-9]. The interesting properties and potential applications of 1D nanomaterials have motivated intensive attention and investigation [10,11]. Due to the unique properties in chemistry, optic, electronics, magnetic, mechanics and other properties of the 1D nanomaterials, they can be applied to compose field effect transistors, bipolar junction transistors, light-emitting diodes (LED), lasers, photodetectors, high sensitivity biological and chemical sensors [12-16].

2. Experimental Part

The chemical etching mechanism is a novel fabricating method of forming large-area uniform silicon nanowires arrays which has been developed over the past few years. Single crystal structure of silicon nanowires can be achieved on the Si samples. The initiating materials are prepared by several kinds of silicon wafers with different doping levels, surface orientations. It is another kind of method that proceeds under room temperature, with the catalysis of silver (Ag) or gold (Au) and the chemical etching was carried out in aqueous solution of hydrofluoric acid (HF) and hydrogen peroxide.(H_2O_2) (see Fig. 1).

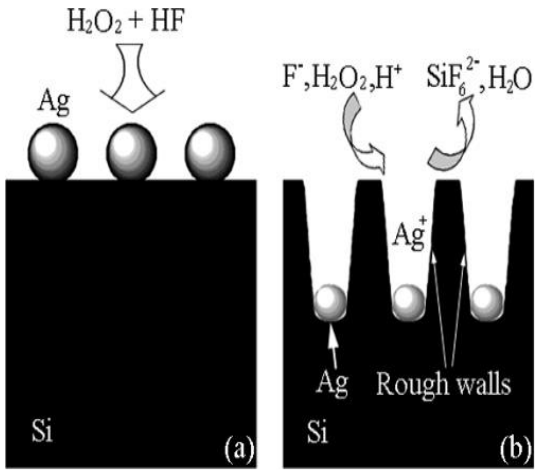

Fig. (1) Schematic elucidations of the formation mechanism of Si nanowires (SiNWs) arrays: (a) at the starting point; (b) during the etching process

The correlated silicon nanowires arrays with different morphologies were acquired. The silicon nanowires have the same type and same doping level of the starting wafer and those on the same wafer have the same orientation. For example, silicon nanowires in the (100) direction was formed by both (100)- and (111)- oriented p-type wafers For every kind of silicon wafer, the factors affecting the etching conditions, as well as compositions of etchant, temperature, and time, were also taken into consideration systematically. This is an adequate method to fabricate a large amount of silicon nanowires with defined type, doping level, and growth direction for industrial use.

First of all, the Si substrates were cut to about 3x3 cm^2, and then were placed into beakers washed with distilled water for several times. Then the substrates were washed with detergent in the ultrasonic machine, after that the substrates were again washed with the acetone in the environment of ultrasonic by ultrasonic washing machine for ten minutes.

In order to eliminate the contaminants and the possible organics on the surface of the samples, they were immersed into the oxidizing agents (H_2SO_4 and H_2O_2) with the volume ratio of 3 to 1 under the room temperature for about 15 minutes. Then the sample were reacted with 4% of HF(aq) to withdraw oxide from the Si samples. The Si substrates were put into a gold coating containing 4.8M HF and 0.001M $HAuCl_4$. After the Si substrates having been stirred slowly with the HF and $HAuCl_4$, a layer of gold nanoparticles were coated on the surface of the substrates, for the purpose of taking away the excessive gold ions, the samples were washed with distilled water and then were etched with a solution containing 4.8 M HF and H_2O_2. The gold nanowires were etched in a dark environment for 30 minutes under room temperature, they were immersed in the dilute HNO_3 solution to take away the gold catalyst. From the observation of the gold silicon nanowires substrates, the obtained surfaces appear black in deep, and their back sides are observed to in gray. The substrates were put to react with the HF again so that the oxide layer can be eliminated and then the samples were cleaned with distilled water under N_2 flow.

3. Results and Discussion

The silicon nanowires (SiNWs) were taken to SEM to study the surface morphology after experiencing the chemical etching process. The electron beam energy and beam spot size limit the resolution. Both large area and local area can be investigated with switching the magnification easily. For some nonconductive substrates, coating a thin film of gold or carbon for measurement is needed.

Figure (2) a shows the SEM images of typical Si wafers coated with a thin layer of gold nanoparticles. Figure (2b) shows SEM image of a partially coated Si wafer. After discussed the schematic illustration of the porous SiNWs synthesis, the main affecting factors in etching would be studied. Figure (2a) shows low magnification of cross section SEM image of the SiNWs from the top view and figure (2b) is the high magnification one.

Figure (3) shows that with the etchant 0.067M H_2O_2+4.8M HF react with p-type wafer, the SiNWs array lengths are uniform.

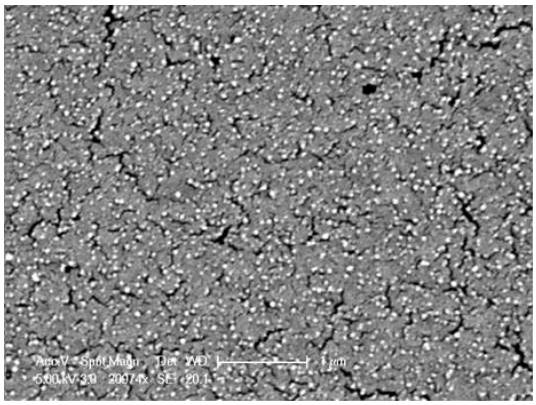

(a)

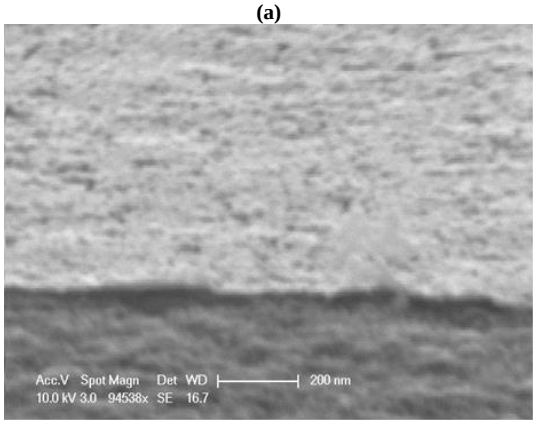

(b)

Fig. (2) SEM image of a typical Si wafer (a) coated with a thin layer of Au nanoparticles, and (b) partially coated Si wafer

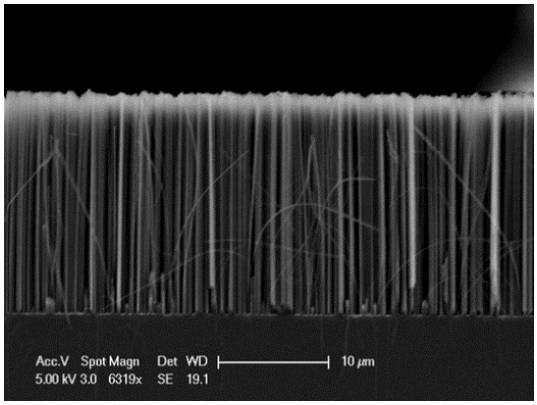

Fig. (3) the SEM image of the cross section area of SiNWs

After that, the concentration of the etchant (H_2O_2 and HF) was varied to see how it can affect the quality of the SiNWs arrays etched. It is assumed that the concentration of the HF is constant and the concentration of the H_2O_2 is variable. It is indicated that when the H_2O_2 increases, the length of the SiNWs arrays start to become nonuniform as these arrays are not evenly distributed as the concentration before. This is because when the concentration of the H_2O_2 increases, the aggregate formed increases and the etching depths increases. If the concentration of H_2O_2 keeps increasing, the etching depths will decrease, that is why the SiNWs arrays start to be aligned uniformly before when first increasing the H_2O_2 and the SiNws arrays aligned non-uniformly at the end. This still holds in the case of having constant concentration of H_2O_2, variable concentration of HF, as shown in Fig. (4).

As can be seen, the SiNWs arrays with the most uniform alignment in the condition of 0.02 M H_2O_2 + 1.2M HF reacting with n-type silicon wafer. The surface area is very large, which is due to formation of huge amount of pore within the SiNWs.

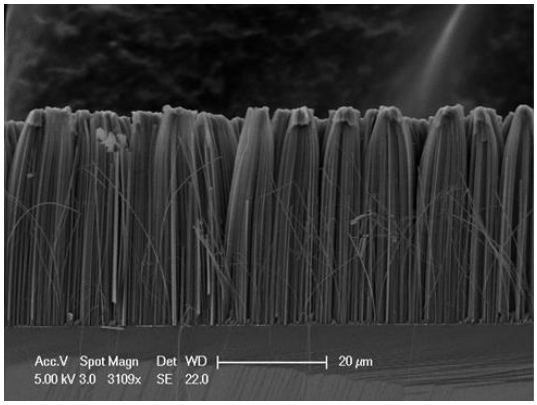

(a)

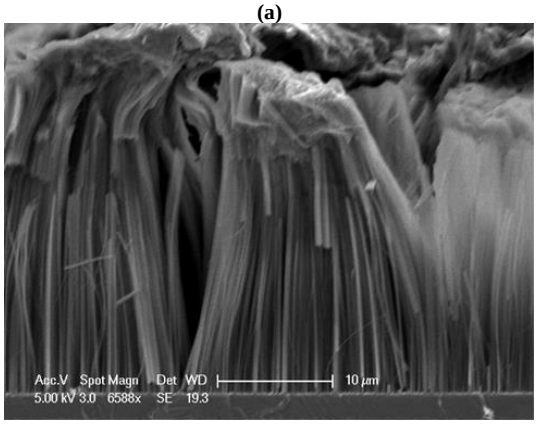

(b)

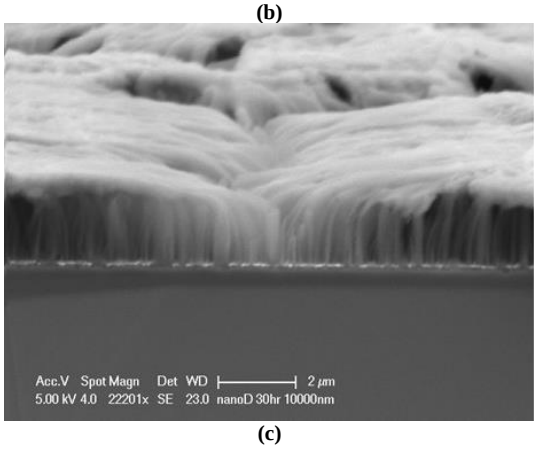

(c)

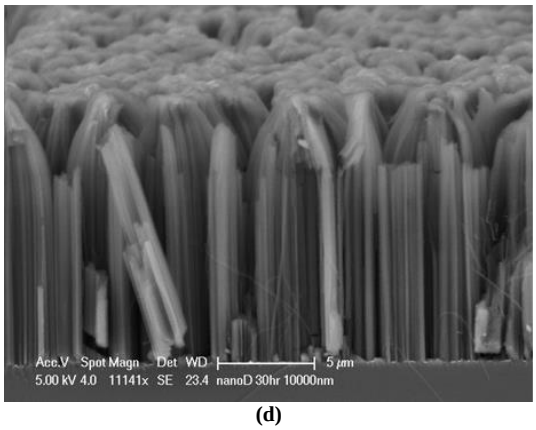

(d)

Fig. (4) SEM images of SiNWs obtained in a mixed solution of (a) H_2O_2 (0.02 M) and HF (4.8 M), (b) H_2O_2 (0.07 M) and HF (4.8 M), (c) H_2O_2 (0.02 M) and HF (1.2 M), and (d) H_2O_2 (0.02 M) and HF (2.4 M)

4. Conclusion

From this work, we can find that the best condition of forming the best quality SiNWs is 0.02M H_2O_2 + 1.2M HF. The increase of concentration of either H_2O_2 or HF can increase the etching depths at the beginning as the aggregate increases, but if the concentration of H_2O_2 or HF keep increasing to a certain amount, the etching depth decrease and the quality of the SiNWs decreases.

References

[1] X. Leng, C. Wang and Z. Yuan, "Progress in metal-assisted chemical etching of silicon nanostructures", *Procedia CIRP*, 89 (2020) 26-32.

[2] T. Kjeldstad et al., "Selective etching of nanostructured a-Si:Al and its effect on porosity, Al gradient and surface oxidation", *Thin Solid Films*, 702 (2020) 137982.

[3] A.A.K. Hadi and O.A. Hamadi, "Optoelectronic Characteristics of As-doped Si Photodetectors Produced by LID Technique", *Iraqi J. Appl. Phys. Lett.*, 1(2) (2008) 23-26.

[4] A.K. Yousif and O.A. Hamadi, "Plasma-Induced Etching of Silicon Surfaces", *Bulg. J. Phys.*, 35(3) (2008) 191-197.

[5] C. Yao et al., "Design and fabrication of wafer-scale highly uniform silicon nanowire arrays by metal-assisted chemical etching for antireflection films", *Results in Phys.*, 31 (2021) 105018.

[6] F. Demami et al., "Silicon nanowires synthesis for chemical sensor applications", *Procedia Eng.*, 5 (2010) 351-354.

[7] O.A. Hamadi, "Profiling of Antimony Diffusivity in Silicon Substrates using Laser-Induced Diffusion Technique", *Iraqi J. Appl. Phys. Lett.*, 3(1) (2010) 23-26.

[8] O.A. Hamadi, B.A.M. Bader and A.K. Yousif, "Electrical Characteristics of Silicon p-n Junction Solar Cells Produced by Plasma-Assisted Matrix Etching Technique", *Eng. Technol. J.*, 26(8) (2008) 995-1001.

[9] O.A. Hamadi, S.M. Hussain, A.A. Hadi and R.O. Mahdi, "Normalized Characteristics of Laser-Induced Diffusion of Arsenic Dopants in Silicon", *Eng. Technol. J.*, 27(4) (2007) 584-590.

[10] O.A. Hammadi and N.E. Naji, "Electrical and spectral characterization of CdS/Si heterojunction prepared by plasma-induced bonding", *Opt. Quantum Electron.*, 48(8) (2016) 375-381.

[11] O.A. Hammadi, "Characteristics of Heat-Annealed Silicon Homojunction Infrared Photodetector Fabricated by Plasma-Assisted Technique", *Phot. Sen.*, 6(4) (2016) 345-350.

[12] O.A. Hammadi, "Photovoltaic Properties of Thermally-Grown Selenium-Doped Silicon Photodiodes for Infrared Detection Applications", *Phot. Sen.*, 5(2) (2015) 152-158.

[13] P.P. Michałowski et al., "Secondary ion mass spectrometry quantification of boron distribution in an array of silicon nanowires", *Measurement*, 211 (2023) 112630.

[14] R.A. Ismail, O.A. Abdulrazaq, A.A. Hadi and O.A. Hamadi, "Characterization of Si p-n Photodetectors Produced by Laser-Induced Diffusion", *Int. J. Mod. Phys.*, 19(31) (2005) 4619-4628.

[15] R.-R. Yang et al., "Silicon nanowire-based energetic materials with significantly improved hygroscopicity", *Energ. Mater. Front.*, 2(2) (2021) 105-110.

Structural Characteristics of Aluminum Nitride Thin Films Prepared by Pulsed-Laser Deposition

Ali M. Jasim, Abbas R. Hussain, Kadhum N. Fezaa

Department of Physics, College of Science, Thi Qar University, Nasiriya, IRAQ

Abstract

In this work, aluminum nitride thin films were prepared and deposited on glass substrates by pulsed-laser deposition technique using different pulse energies. The structural characteristics of the films were introduced and analyzed. The crystalline structure of the prepared films was found to be polycrystalline and dependent on the laser pulse energy. Also, the minimum particle size on the film surface is highly dependent on the laser pulse energy as a minimum particle size of 125nm was produced when laser pulse energy of 100mJ was used. The surface roughness of the prepared films was found to depend on the laser pulse energy and it was increased from 1 to 5.3nm as the laser pulse energy was increased from 0.1 to 100mJ.

Keywords: Titanium dioxide; Nanoparticles; Structural phase; Reactive sputtering; Solvothermal method
Received: 17 May 2023; **Revised:** 11 June 2023; **Accepted:** 18 June 2023; **Published:** 1 September 2023

1. Introduction

Epitaxially grown thin film crystalline aluminum nitride is used for surface acoustic wave sensors (SAWs) deposited on silicon wafers because of AlN's piezoelectric properties [1-3]. One application is an RF filter, widely used in mobile phones [4,5], which is called a thin-film bulk acoustic resonator (FBAR). This is a MEMS device that uses aluminum nitride sandwiched between two metal layers [6,7].

AlN is also used to build piezoelectric micro-machined ultrasound transducers, which emit and receive ultrasound and which can be used for in-air rangefinding over distances of up to a meter [8-10].

Metallization methods are available to allow AlN to be used in electronics applications similar to those of alumina and beryllium oxide [11]. AlN nanotubes as inorganic quasi-one-dimensional nanotubes, which are isoelectronic with carbon nanotubes, have been suggested as chemical sensors for toxic gases [12,13].

Currently there is much research into developing light-emitting diodes to operate in the ultraviolet using gallium nitride based semiconductors and, using the alloy aluminum gallium nitride, wavelengths as short as 250 nm have been achieved. In 2006, an inefficient AlN LED emission at 210 nm was reported [14-16].

AlN-based high electron mobility transistors (HEMTs) have attracted a high level of attention due to AlN's superior properties, such as better thermal management, reduced buffer leakage, and excellent integration for all nitride electronics [17]. AlN buffer layer is a critical building block for AlN-based HEMTs, and it has been grown by using MOCVD or MBE on different substrates [18]. Building on top of AlN buffer, n-channel devices with 2D electron gas (2DEG) and p-channel devices with 2D hole gas (2DHG) have been demonstrated. The combination of high-density 2DEG and 2DHG on the same semiconductor platform makes it a potential candidate for CMOS devices [19].

Among the applications of AlN are optoelectronics, dielectric layers in optical storage media, electronic substrates, chip carriers where high thermal conductivity is essential, military applications, as a crucible to grow crystals of gallium arsenide, and steel and semiconductor manufacturing [20].

In this work, aluminum nitride thin films were prepared and deposited on glass

substrates by pulsed-laser deposition technique using different pulse energies. The structural characteristics of the films were introduced and analyzed.

2. Experimental Part

A pulsed-laser deposition technique was used to deposit AlN thin films on glass substrates inside an evacuated chamber. This chamber was initially evacuated down to 10^{-3} mbar using a double-stage rotary pump. The AlN target of 5cm diameter was placed on a holder in order the laser beam is incident on this target with an angle of 45°. A Q-switched Nd:YAG laser of 532nm wavelength, 1J maximum energy, 5ns pulse duration and 10Hz pulse repetition rate was used. The experimental setup used in this work is shown in Fig. (1).

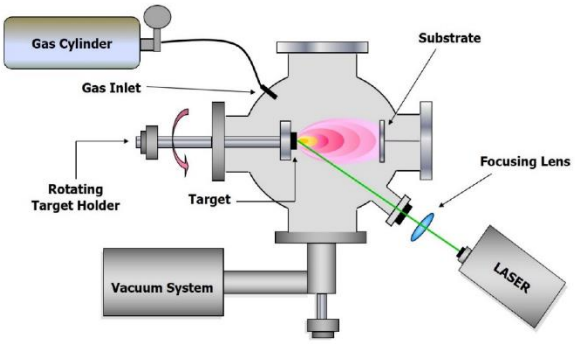

Fig. (1) The experimental setup used in this work

As different values of laser pulse energies were used to irradiate the AlN target, the crystalline structure of the deposited thin films was determined by the x-ray diffraction (XRD) as a function of laser pulse energy. As well, the surface morphology of the nanostructured films was determined by the field-emission scanning electron microscopy (FE-SEM) and atomic force microscopy (AFM).

3. Results and Discussion

Figure (2) shows the XRD patterns of four AlN samples prepared using four different laser pulse energies (0.1, 1, 10 and 100mJ). It is clear that increasing laser pulse energy leads to support the growth of the <002> crystalline orientation on the account of the crystalline orientation <101>, while the growth of the <102> crystalline orientation is not uniformly dependent on the laser pulse energy. Also, the crystalline orientation was totally disappeared as the laser pulse energy was increased to 100mJ. These results can be attributed to the fact that higher pulse energy does not allow crystalline orientation of lower growth probability to grow and only the crystalline orientation of the highest growth probability is allowed to grow.

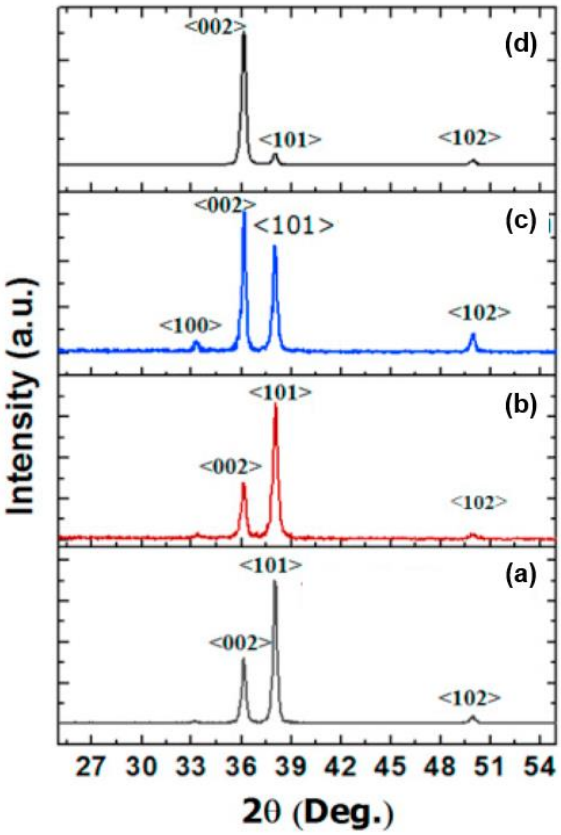

Fig. (2) XRD patterns of the AlN thin film samples prepared in this work using laser pulse energy of (a) 0.1mJ, (b) 1mJ, (c) 10mJ, and (d) 100mJ

Figure (3) shows the FE-SEM image of the AlN sample prepared using laser pulse energy of 100mJ. The majority of particles have approximately polygon shape. The minimum particle size is 125 nm while larger particles can be clearly seen in this image. This is ascribed to the higher pulse energy that can eject grains from larger volume when compared to the lower pulse energies. These grains would attach together to form large particles before deposited on the substrate. The experiments showed that

using lower pulse energies can produce smaller particles but with more crystalline orientations, as was confirmed by the XRD patterns (Fig. 2). Table (1) summarizes the effect of laser pulse energy on the crystallite size determined from the XRD patterns by Scherrer's formula and minimum particle size determined from the FE-SEM results.

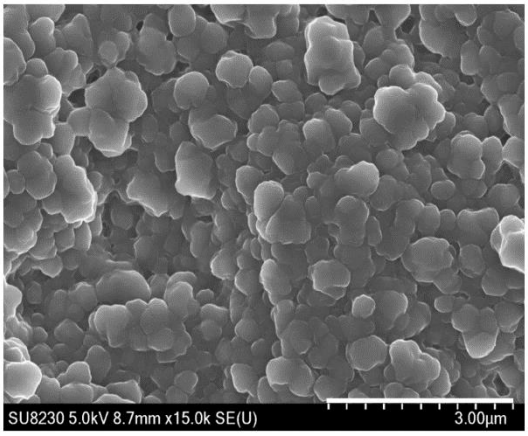

Fig. (2) SEM image of the AlN nanopowder sample prepared in this work using pulse energy of 100mJ

Table (1) Effect of laser pulse energy on nanoparticle size of AlN samples prepared in this work

Sample	Pulse Energy (mJ)	Crystallite Size (nm)	Minimum Particle Size (nm)
(a)	0.1	61.5	19
(b)	1	22.6	26
(c)	10	16.0	73
(d)	100	22.8	125

To further investigate the nanostructure of the AlN thin films, AFM was utilized to look at the surface morphology. Figure (4) shows AFM surface height images for each of the films prepared in this study. The AlN thin films exhibited high RMS surface roughnesses of 5.3 nm. The high surface roughness was primarily due to the presence of small surface particles which may be evidence of either gas phase nucleation during growth or AlN crystallite formation during the post deposition rapid thermal effect as a result of irradiation of AlN target with laser pulses. Excluding the surface particles, the calculated RMS surface roughness is reduced to 1nm. We also note that prior AFM measurements of thinner (3-5nm) amorphous films show an RMS roughness of <0.2nm. Concerning the PLD-prepared AlN film, the RMS surface roughness of 5.3 nm is slightly higher than, but consistent with, the RMS surface roughness values reported previously [8,10,18]. Specifically, the RMS surface roughness was increased from 1 to 5.3nm as the laser pulse energy was increased from 0.1 to 100mJ. Thus, the high surface roughness for our AlN thin films can be partially attributed to the high deposition temperature as a result of high pulse energy and the comparatively high thickness of 200nm.

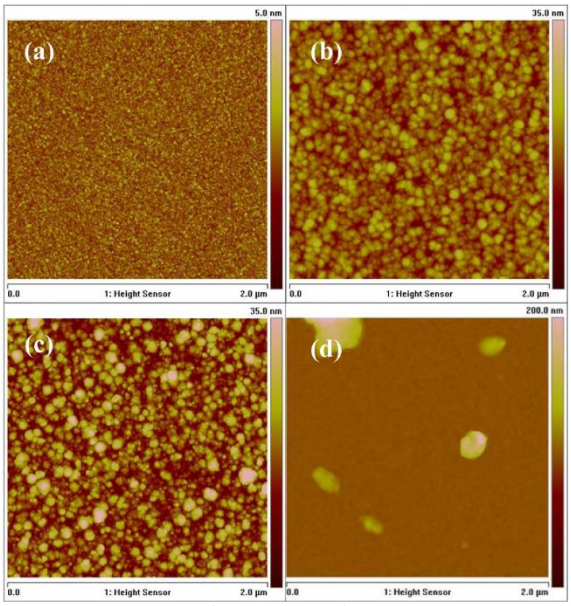

Fig. (4) AFM images of the AlN thin film samples prepared in this work using laser pulse energy of (a) 0.1mJ, (b) 1mJ, (c) 10mJ, and (d) 100mJ

4. Conclusion

In concluding remarks, aluminium nitride thin films can be prepared by pulsed-laser deposition technique. These thin films are polycrystalline with reasonable control by the pulse energy to support certain crystalline orientations and suppress others. The prepared thin films can contain nanostructures but the particle size within these films is increased with increasing laser pulse energy due to the role of higher energies to eject more grains from the target and hence form larger particles.

References

[1] R. Couturier et al., "Elaboration and characterization of a metal matrix composite:

Al/AlN", J. Eur. Ceram. Soc. 17 (1997) 1861-1866.
[2] F. Roulet et al., "Corrosion behaviour of aluminium nitride in liquid aluminium: Influence of the microstructure", J. Eur. Ceram. Soc. 17 (1997) 1877-1883.
[3] J. Jarrige et al., "Effect of oxygen on the thermal conductivity of aluminium nitride ceramics", J. Eur. Ceram. Soc. 17 (1997) 1891-1895.
[4] A.V. Virkar, T.B. Jackson and R.A. Cutler, "Thermodynamic and Kinetic Effects of Oxygen Removal on the Thermal Conductivity of Aluminum Nitride", J. Am. Ceram. Soc. 72 (1989) 2031-2042.
[5] T. Yano et al., "Neutron irradiation effects on isotope tailored aluminum nitride ceramics by a fast reactor up to 2×10^{26} n/m^2", J. Nucl. Mater. 329-333 (2004) 1471-1475.
[6] T. Yano and T. Iseki, "A HREM study of neutron-irradiation-induced dislocations in aluminum nitride", Philos. Mag. Lett. 62 (1990) 83-87.
[7] T. Yano, H. Miyazaki and T. Iseki, "Effect of isochronal annealing on thermal diffusivity of neutron-irradiated AlN", J. Nucl. Mater. 230 (1996) 74-77.
[8] T. Yano et al., "Macroscopic length, lattice-parameter and microstructural changes in neutron-irradiated aluminum nitride due to annealing", J. Nucl. Mater. 191 (1992) 635-639.
[9] C.S. Kim et al., "Mechanical-properties of neutron-irradiated AlN", J. At. Energy Soc. Jpn. 34 (1992) 335-341.
[10] T. Yano and T. Iseki, "Swelling and microstructure of AlN irradiated in a fast-reactor", J. Nucl. Mater. 203 (1993) 249-254.
[11] F. Porte et al., "Thermoluminescence of aluminium nitride: Influence of the thermal treatment", J. Eur. Ceram. Soc. 17 (1997) 1797-1802.
[12] M. Benabdesselam et al., "Thermoluminescence of AlN. Influence of synthesis processes", J. Phys. Chem. 99 (1995) 10319-10323.
[13] L. Trinkler et al., "Thermoluminescence properties of AlN ceramics", Radiat. Meas. 29 (1998) 341-348.
[14] A.L. Martin et al., "Visible emission from amorphous AlN thin-film phosphors with Cu, Mn, or Cr", J. Vac. Sci. Technol. A: Vac Surf. Films 19 (2001) 1894-1897.
[15] K. Kawabe, R.H. Tredgold and Y. Inuishi, "Electrical and optical properties of AlN - a thermostable semiconductor", Electr. Eng. Jpn. 87 (1967) 62-70.
[16] G.A. Cox et al., "On the preparation, optical properties and electrical behaviour of aluminium nitride", J. Phys. Chem. Solids 28 (1967) 543-548.
[17] T. Mattila and R.M. Nieminen, "*Ab initio* study of oxygen point defects in GaAs, GaN, and AlN", Phys. Rev. B 54 (1996) 16676-16682.
[18] M. Bickermann, B.M. Epelbaum and A. Winnacker, "Characterization of bulk AlN with low oxygen content", J. Cryst. Growth 269 (2004) 432-442.
[19] J. Pasternak and L. Roskovcova, "Optical absorption end of AlN single crystals", Phys. Status Solidi 26 (1968) 591.
[20] G.A. Slack et al., "Some effects of oxygen impurities on AlN and GaN", J. Cryst. Growth 246 (2002) 287-298.

Effect of Target Conductivity Type on Optical Constants of Silicon Nitride Thin Films Prepared by DC Reactive Sputtering

Diyar A. Taher, Mohammed A. Hameed

Department of Physics, College of Science, University of Baghdad, Baghdad, IRAQ

Abstract

In this work, the effect of electrical conductivity type of the silicon target used to prepare silicon nitride thin films on glass substrates by dc reactive sputtering technique was studied. Two silicon wafers different in the type of electrical conductivity (n-type and p-type) were used as sputtering target. Two different gas mixing ratios (50:50 and 70:30) as well as two different deposition times (1:30 and 3 hours) were considered for comparison between the optical constants, mainly refractive index, extinction coefficient, real and imaginary parts of refractive index, of the prepared films. In general, thin films prepared after deposition time of 3 hours have shown much more uniform behaviors of their optical constants. The effect of type of conductivity of the silicon target was not clearly observed in the films deposited after shorter time but it was clearly observed in the films deposited after longer time as the films prepared from p-type target have shown higher values of optical constants.

Keywords: Silicon nitride; Optical constants; Reactive sputtering; Thin films
Received: 02 May 2023; **Revised:** 05 June 2023; **Accepted:** 09 June 2023; **Published:** 1 September 2023

1. Introduction

Silicon nitride thin films and nanostructures have found increasing research interest within the last three decades due to the increasing applications based on these structures [1]. These applications are various to include high-temperature coatings and devices, high-hardness coatings, functional materials, wide bandgap devices, biomedical parts and coatings, etc [2-7]. Therefore, the properties and characteristics of such thin films or nanostructures are of extraordinary importance for the intended application. For example, photonics applications require reasonably high uniformity of optical properties of silicon nitride thin films in order to ensure the optimum optical performance [8-10]. Similarly, biomedical applications may require high uniformity of optical, electrical and mechanical characteristics especially when such thin films and nanostructures are employed inside the human body, such as bone restoration, joints, anti-friction surfaces, and ion release inhibitors [11-15]. Silicon nitride is an excellent candidate material for biomedical applications mainly due to its biocompatibility and non-toxicity [16].

In this work, two silicon wafers different in the type of electrical conductivity (n-type and p-type) as well as two different gas mixing ratios were used to deposit silicon nitride thin films on glass substrates by dc reactive sputtering technique in order to study their effects on the optical constants of the prepared films.

2. Experimental Part

Silicon nitride thin films were deposited on glass substrates using dc reactive magnetron sputtering technique. In this technique, gas mixtures of argon and nitrogen with two different mixing ratios (50:50 and 70:30) were used. Two silicon targets with different types of conductivity (n-type and p-type) were used. The deposition chamber was initially evacuated down to 0.001 torr. Deposition process was carried out at room temperature using gas

mixture pressure of 0.8 torr, discharge voltage of 730V, and discharge current of 50mA. Deposition time was 4 hours for all samples. More details on the optimum preparation conditions can be found elsewhere [25-29,34].

The absorption spectra of the prepared thin films were recorded in the spectral range 200-1000nm using a SpectraAcademy SV2100 spectrophotometer.

3. Results and Discussion

Figure (1) shows the variation of refractive index with wavelength (dispersion relationship) for the silicon nitride prepared in this work after deposition time of 1:30 hours. It is clear that the film prepared from the n-type Si target using 50:50 gas mixing ratio shows higher values (1.75-2.15) of refractive index than other films whose values of refractive index are ranging in 1.5-1.8. As refractive index expresses the density of the grown film, then the availability of nitrogen in the gas mixture (50%) in addition to the higher tendency of n-type Si atoms for bonding may cause the formation of Si_3N_4 film with larger thickness, and hence higher refractive index.

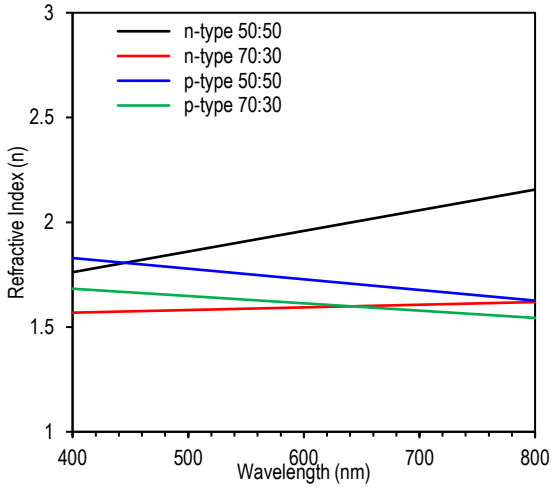

Fig. (1) Variation of refractive index with wavelength of the Si_3N_4 thin films deposited after 1:30 hours

The other important note that can be observed from this result is the increasing refractive index of the films prepared from n-type Si target with wavelength while the refractive index of the films prepared from p-type Si target is decreasing with wavelength. This may be attributed to the fact that the Si_3N_4 thin films prepared from p-type Si target may contain some voids in their structure as the sputtered Si atoms have holes as the majority charge carriers, which impose different structure for the prepared thin films.

As the extinction coefficient indicates the amount of attenuation when the electromagnetic wave propagates through the material, so the Si_3N_4 thin films prepared from n-type Si target using 50:50 gas mixing ratio exhibit higher attenuation to the visible wavelengths, while other films can be described with moderate attenuation.

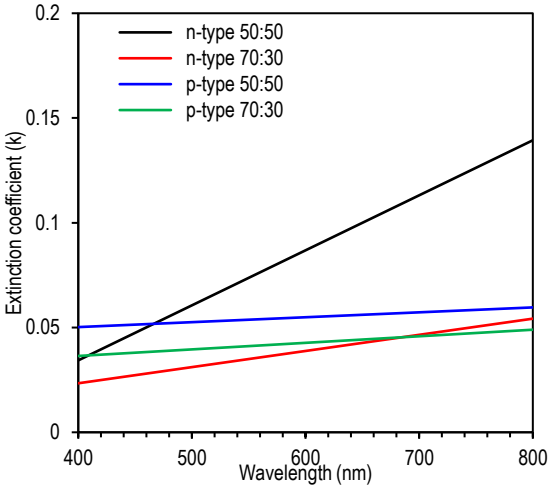

Fig. (2) Variation of extinction coefficient with wavelength of the Si_3N_4 thin films deposited after 1:30 hours

The real and imaginary parts of refractive index shown in Fig. (3) show the same difference between Si_3N_4 thin films prepared from the n-type Si target with respect to those prepared from the p-type Si target. Regardless the effect of gas mixing ratio, the type of conductivity of the silicon target has an important role in determining the structure of the prepared films and hence their optical properties. Obviously, the optical constants of silicon are dependent on the doping concentration and of course on the nature of the dopants.

Figure (5) shows the variation of refractive index with wavelength (dispersion relationship) for the silicon nitride prepared in this work after deposition time of 3 hours. In contrast to the results in Fig. (1), it is clear that the film prepared from p-type Si target

using 70:30 gas mixing ratio shows higher values (~2.55) of refractive index than other films whose values of refractive index are ranging in 1.5-2.1. The reason of this result is definitely different from that proposed for the result in Fig. (1). Here, Si_3N_4 thin films prepared from p-type Si target regardless the gas mixing ratio may have higher stability than those prepared from n-type Si target as the majority carries (holes) have recombined with electrons shared with N atoms during bonding process to form the Si_3N_4 molecules. This may lead to grow more layers during the deposition time and hence higher values of refractive index are obtained.

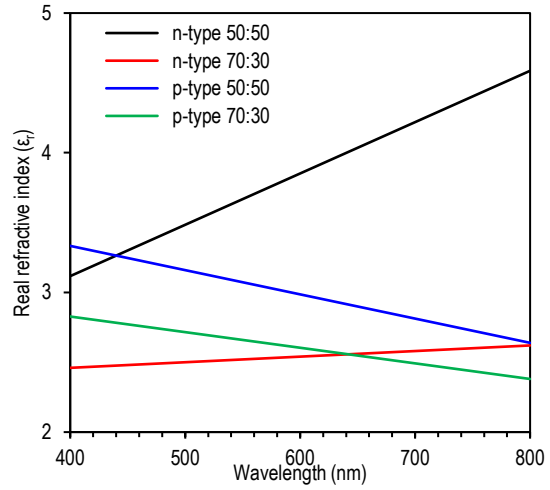

Fig. (3) Variation of real part (a) and imaginary part (b) of refractive index with wavelength of the Si_3N_4 thin films deposited after 1:30 hours

Similar interpretation can be proposed for the result of extinction coefficient shown in Fig. (5) as the films prepared from p-type target can attenuate the light uniformly over the visible range. Hence, the optical performance of these films can be considered better than those prepared from n-type target.

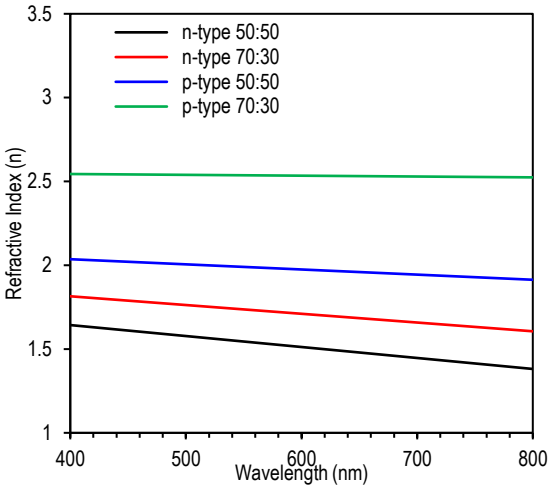

Fig. (4) Variation of refractive index with wavelength of the Si_3N_4 thin films deposited after 3 hours

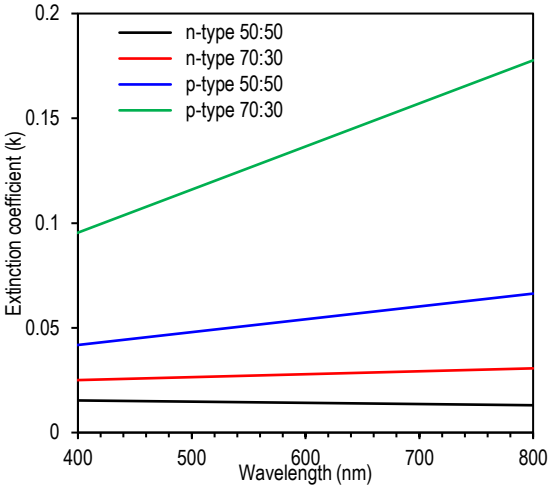

Fig. (5) Variation of extinction coefficient with wavelength of the Si_3N_4 thin films deposited after 3 hours

The real and imaginary parts of refractive index shown in Fig. (6) may confirm the results presented in figures (4) and (5). Accordingly, the optical properties of the Si_3N_4 thin films deposited after 3 hours can be much more uniform than those deposited after 1:30 hours. As well, the films prepared from p-type target can be better than those prepared from n-type target as they show higher values of both real and imaginary parts of refractive index. However, in both cases, the real part of refractive index decreases with wavelength while the

imaginary part increases with wavelength. This behavior can be a feature for the films prepared after longer deposition times.

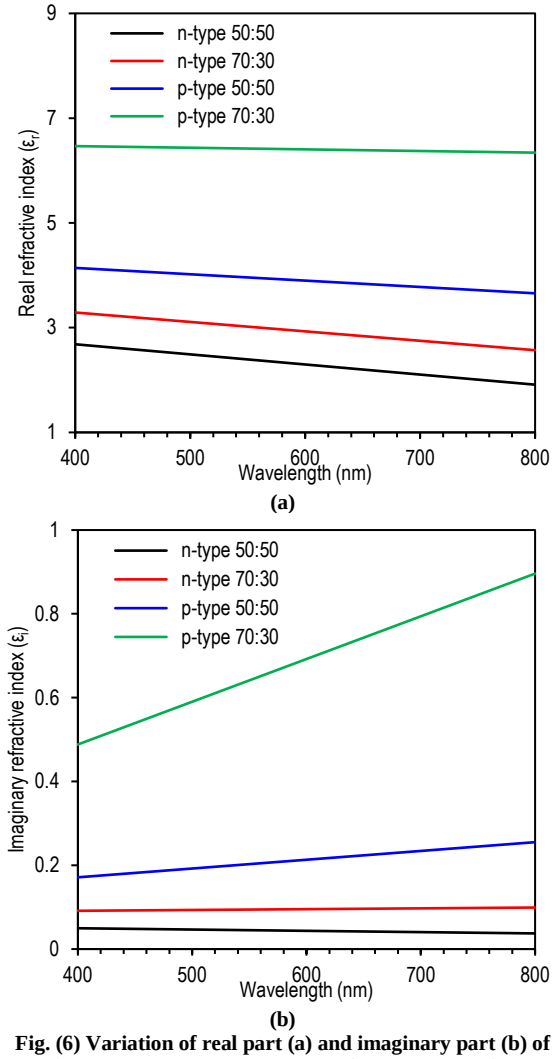

Fig. (6) Variation of real part (a) and imaginary part (b) of refractive index with wavelength of the Si_3N_4 thin films deposited after 1:30 hours

4. Conclusion

In concluding remarks, the effect of electrical conductivity type of the Si target used to prepare Si_3N_4 thin films on glass substrates by dc reactive sputtering technique was studied. The optical constants of the prepared films are highly dependent on the type of target conductivity as well as the gas mixing ratio. Therefore, the application determines the required optical properties of the Si_3N_4 thin films, especially when the film uniformity is an important requirement.

References

[1] F.J. Kadhim and A.A. Anber, "Microhardness of Nanostructured Si_xN_{1-x} Thin Films Prepared by Reactive Magnetron Sputtering", Iraqi J. Appl. Phys., 12(2) (2016) 15-19.

[2] O.A. Hammadi, M.K. Khalaf and F.J. Kadhim, "Fabrication and Characterization of UV Photodetectors Based on Silicon Nitride Nanostructures Prepared by Magnetron Sputtering", Proc. IMechE, Part N, J. Nanomater. Nanoeng. Nanosys., 230(1) (2016) 32-36.

[3] F.J. Kadhim and A.A. Anber, "Fabrication of nanostructured silicon nitride thin film gas sensors by reactive direct current magnetron sputtering", Proc. IMechE, Part N, J. Nanomater. Nanoeng. Nanosys., 231(4) (2017) 173-178.

[4] F.J.Kadhim and A.A. Anber, "Fabrication of Nanostructured Silicon Nitride Films by Reactive DC Magnetron Sputtering for Gas Sensing Applications", Proc. IMechE, Part N, J. Nanoeng. Nanosys., 231(4) (2017) 173-178.

[5] B.K. Nasser and M.A. Hameed, "Narrow Emission Linewidth of Highly-Pure Silicon Nitride Nanoparticles in Different Dye Solutions as Random Gain Media", Nonl. Opt. Quant. Opt., 35(1-2) (2020) 99-105.

[6] O.A. Hammadi, "New Technique to Synthesize Silicon Nitride Nanopowder by Discharge-Assisted Reaction of Silane and Ammonia", Mater. Res. Exp., 8(8) (2021) 085013.

[7] O.A. Hammadi, M.K. Khalaf and F.J. Kadhim, "Silicon Nitride Nanostructures Prepared by Reactive Sputtering Using Closed-Field Unbalanced Dual Magnetrons", Proc. IMechE, Part L, J. Mater.: Design and Applications, 231(5) (2017) 479-487.

[8] A.A. Anber and F.J. Kadhim, "Preparation of Nanostructured Si_xN_{1-x} Thin Films by DC Reactive Magnetron Sputtering for Tribology Applications", Silicon, 10(3) (2018) 821-824.

[9] B.K. Nasser and M.A. Hameed, "Structural Characteristics of Silicon Nitride Nanostructures Synthesized by DC Reactive Magnetron Sputtering", Iraqi J. Appl. Phys., 15(4) (2019) 33-36.

[10] F.J. Kadhim, O.A. Hammadi and A.A. Anber, "Spectroscopic Study of Chromium-Doped Silicon Nitride Nanostructures Prepared by DC Reactive Magnetron Sputtering", Iraqi J. Appl. Phys., 17(2) (2021) 9-12.

[11] O.A. Hammadi, M.K. Khalaf, F.J. Kadhim and B.T. Chiad, "Operation Characteristics of a Closed-Field Unbalanced Dual-Magnetrons Plasma Sputtering System", Bulg. J. Phys., 41(1) (2014) 24-33.

Structural and Morphological Characteristics of Cadmium Doped Titanium Dioxide Thin Films Prepared by Spray Pyrolysis

Selma M. Hussain

Department of Applied Physics, University of Technology, Baghdad, IRAQ

Abstract

Undoped and doped cadmuim titanium oxide thin films at different percentage (1, 3, 4, and 5) % were fabricated by spray pyrolysis by using a solution of titanium tetrachloride and ethyl alcohol. The films have been deposited on heated quartz substrates at 623 K. After annealing for 120 min at 823 K, the initially amorphous films became polycrystalline with a predominant anatase structure and average crystallite sizes depending on dopant Cd concentration. Atomic force microscope (AFM) results show that the addition of the Cd to TiO2 thin films become smooth. Photocatalytic activity of the TiO2 films were studied by monitoring the degradation of aqueous methylene blue under UV light irradiation and was observed that increasing doping concentration had good photocatalytic activity which was explained as due to the structural and morphological properties of the films.

Keywords: Titanium dioxide; Nanostructures; Cadmium dopants; Spray pyrolysis
Received: 11 April 2023; **Revised:** 21 June 2023; **Accepted:** 28 June 2023; **Published:** 1 September 2023

1. Introduction

Over the last few years a great attention has been focused on the titanium dioxide (TiO_2) thin films because its excellent materials in many applications, such as in the field of sensors, antireflection coatings, gas sensors [1], solar cells [2] and photocatalysis [3,4]. By doping, especially with transition metal atoms, these properties can be improved as desired, while keeping the films chemical and mechanical stability [1]. There are many methods that can be used to prepare TiO_2 thin films with desired properties including sol–gel [4-7], sputtering [8], anodic oxidation [9-14], pulsed-laser deposition (PLD) [15], and spray pyrolysis [16-18]. Amongst all methods, spray pyrolysis is widely used because of its simplicity, cheap chemical deposition procedure, allowing the growth of rough-surface films at atmospheric pressure, on large area. By this method, dopants can be easily introduced into the matrix of the film by using appropriate precursors [1,16].

In this paper we have investigated the effect of cadmium doping on structural and photocatalytic properties of Cd-doped TiO_2 thin films prepared by spray pyrolysis.

2. Experimental Part

Undoped and cadmium-doped titanium oxide thin films were deposited on heated quartz substrate (623 K), by spraying an appropriate solution from a sprayer, placed at 30 cm in front of the heated substrate holder. The starting solution was prepared by using (2 ml) titanium tetrachloride ($TiCl_4$, purity 99.9%, 1.726g/cm^3 density) dissolved in (20 ml) ethyl alcohol (96%). Filtered air was used as a carrier gas, the deposition time was set to 5 s, the (undoped and doped) samples were annealed at 823 K in air for 120 min. Salt[$CdCl_2.6H_2O$] are used to dope TiO_2 films for different percentages (1,3,4 and 5%) of dopant.

The structural properties of the prepared films were studied by scanning electron microscopy (SEM) type VEGA TESCAN equipment operated at 30 keV. The AFM studies were performed using a scanning probe microscopy (CSPM-5000).

The photocatalytic activity of TiO_2 films was evaluated from the degradation of methylene blue (MB) during its catalytic decomposition. The MB ($C_{16}H_{18}C_lN_3S$) is an organic water soluble cationic dye found in waste waters and is potentially toxic. An aqueous solution of MB (100 mg/l) was taken in the reactor and was constantly stirred. The pH of the solution was adjusted to 3 with dilute hydraulic acid was added. The quartz slide coated with TiO_2 film of area 4.5 cm^2 was immersed in to the MB solution. Initially the MB solution with TiO_2 film was kept in dark for 30 min to establish adsorption–desorption equilibrium. After this stabilization period the TiO_2 film was irradiated with ultraviolet (UV) light source with central wavelength emission at 365 nm. The absorbance of the MB solution was monitored at intervals of 30 min using a UV–Vis spectrophotometer. The rate of photodegradation of MB solution in the case of each film was analyzed by monitoring the intensity variation of the main absorption band of MB at 605 nm.

3. Results and Discussion

Figure (1) shows the surface morphology micrographs of undoped and Cd-doped TiO_2 thin films measured by scanning probe microscope with contact mode. It exhibits that all samples have dense grains. The grains are basically round, which grow preferentially along the c-axis orientation perpendicular to the substrates. For the pure TiO_2 thin film as show in Fig. (3a), the average grain size is about 140 nm and the lateral size distribution is not uniform. The grain size greatly reduces with Cd doping concentration increases. 5% Cd-doped TiO_2 thin film has uniform and dense grains.

AFM results show that by the addition of the Cd to TiO_2 thin films they become smooth where the root mean square (RMS) for undoped and doped with Cd are 0.1658 nm and 0.115 nm respectively. This result agrees well with literature [20].

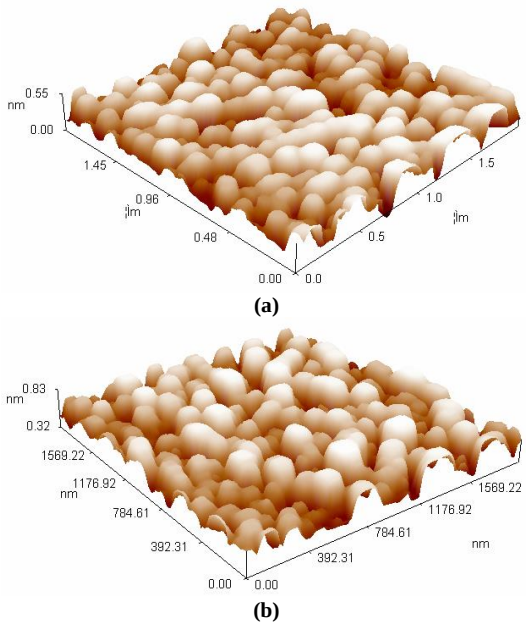

Fig. (1) The AFM images of (a) undopped TiO_2 films, and (b) 5% Cd-doped TiO_2 film

Figure (2) shows the scanning electron microscope (SEM) micrographs of undoped and Cd-doped TiO_2 thin films. The more uniform polyhedral particles of doped TiO_2 could be attributed to slower deposition rate and inhomogeneous nucleation that favor the polyhedral-shaped particles [21]. Films are homogenous and continuous separate coating layers. There seems to be mismatch in average size of crystal determined through Scherer's calculation utilizing XRD data and SEM analysis. SEM image suggest size of crystal to be much larger. It seems appropriate to consider that the particle which appears in SEM images is, in fact, grain agglomerates [22].

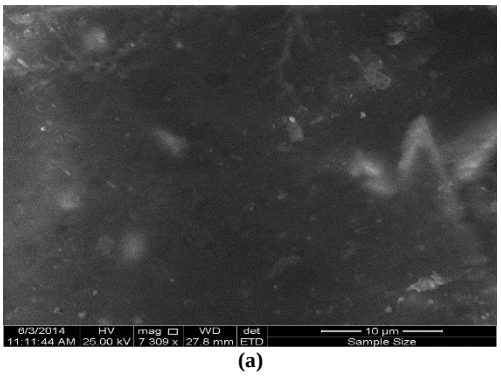

(a)

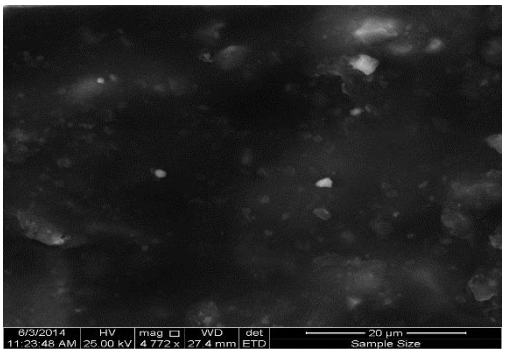

(b)

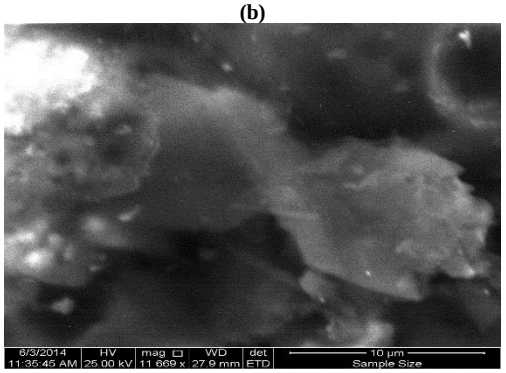

(c)

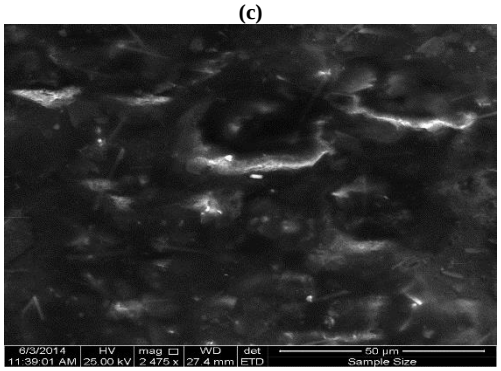

(d)

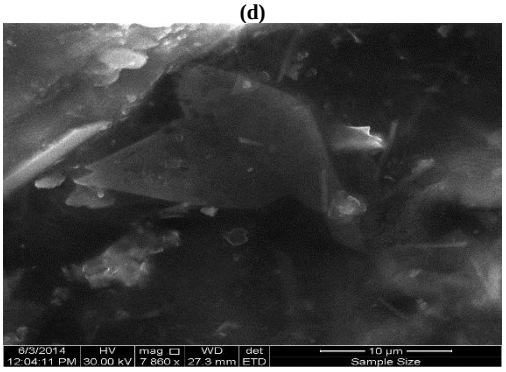

(e)

Fig. (2) SEM images of (a) undoped TiO_2 thin films (b) 1% Cd-doped TiO_2 thin films, (c) 3% Cd-doped TiO_2 thin films, (d) 4% Cd-doped TiO_2 thin films, and (e) 5% Cd-doped TiO_2 thin films

4. Conclusion

Titanium oxide thin films were prepared by spray pyrolysis technique on quartz substrate at 623 K and the effect of Cd doping on structural properties of these thin films was studied by AFM and SEM. The grain size showed dependence on doping concentration as the addition of the Cd to the TiO_2 thin films made them smoother.

References

[1] D. Mardare et al., "Undoped and Cr-doped TiO_2 thin films obtained by spray pyrolysis", *Thin Solid Films*, 518 (2010) 4586-4589.

[2] I. Oja et al., "Structural and electrical characterization of TiO_2 films grown by spray pyrolysis", *Thin Solid Films*, 515 (2005) 674-677.

[3] L. Andronic, S. Manolache and A. Duta, "TiO_2 thin films prepared by spray pyrolysis deposition (SPD) and their photocatalytic activities", *J. Optoelectron. Adv. Mater.*, 9 (2007) 1403-1406.

[4] N.R. Mathews et al., "TiO_2 thin films – Influence of annealing temperature on structural, optical and photocatalytic properties", *Solar Energy*, 83 (2009) 1499–1508.

[5] T. Maiyalagan, B. Viswanathan and U.V. Varadaraju, "Fabrication and characterization of uniform TiO_2 nanotube arrays by sol-gel template method", *Bull. Mater. Sci.*, 29 (2006) 705-708.

[6] K.K. Saini et al., "Structural and optical properties of TiO_2 thin films derived by sol-gel dip coating process", *J. Nano-Cryst. Solid*, 353 (2007) 2469-2473.

[7] T.-S. Kang et al., "Fabrication of highly-ordered TiO_2 nanotube arrays and their use in dye-sensitized silar cells", *Nano Lett.*, 9 (2009) 601-606.

[8] Z. Can et al., "Influences of working pressure on properties for TiO_2 films deposited by DC pulse magnetron sputtering", J. Environ. Sci., 21 (2009) 741–744,.

[9] Y.-K. Lai et al., "Nnitrogen-doped TiO_2 nanotube array films with enhanced photocatalytic activity under various light sources", *J. Hazard. Mater.*, 184 (2010) 855-863.

[10] Y. Tang et al., "The formation of micrometer-long TiO_2 nanotube arrays by anodization of titanium film on conducting glass substrate", *Adv. Nat. Nanosci. Nanotech.*, 2 (2011) 1-7.

[11] L.-L. Li et al., "Morphologic characterization of anodic titania nanotube arrays for dye-sensitized solar cells", *J. Chin. Chem. Soc.*, 27 (2010) 1147-1150,.

[12]H.F. Lu et al., "Amorphous TiO_2 nanotube arrays for low-temperature oxygen sensors", *Nanotechnol.*, 19 (2008) 1-7.

[13] L.-L. Li et al., "Fabrication of long TiO_2 nanotube arrays in a short time using a hybrid anodic method for highly efficient dye-sensitized solar cells", *J. Mater. Chem.*, 20 (2010) 2753-2758.

[14] Y. Lai et al., "Self-organized TiO_2 nanotubes in mixed organic-inorganic electrolytes and their photoelectrochemical performance", *Electrochimica Acta*, 54 (2009) 6536-6542.
[15] M.P. Moreta et al., "Brookite-rich titania lms made by pulsed laser deposition", *Thin Solid Films*, 366 (2000) 8-10.
[16] H.P. Deshmukh, P.S. Shinde and P.S. Patil, "Structural, optical and electrical characterization of spray-deposited TiO_2 thin films", *Mater. Sci. Eng. B*, 130 (2006) 220-227.
[17] I. Oja et al., "Properties of TiO_2 films prepared by the spray pyrolysis method", *Solid State Phenom.*, 99-100 (2004) 259-264.
[18] S.T. Shishiyanu, T.S. Shishiyanu and O.I. Lupan, "Sensing characteristics of tin-doped ZnO thin films as NO_2 gas sensor", *Sensors Actuators B*, 107 (2005) 379–386.
[19] S. Pawar et al., "Effect of annealing on structural, morphological, electrical and optical properties of nanocrystalline TiO_2 thin films", *J. Nano-Electron. Phys.*, 1 (2011) 185-192.
[20] I. Vaiciulis et al., "On Titanium Dioxide spray deposited thin films for soler cells applications", *Proc. Roman. Acad.*, 13(4) (2012).
[21] S.G. Pawar et al., "Effect of annealing on structure, morphology, electrical and optical properties of nanocrystalline TiO_2 thin films", *J. Nano-Electron. Phys.*, 3(1) (2011) 185-192.
[22] M. Mohammadi et al., "Characterization of nanostructured Nd-Doped TiO_2 thin film synthesized by spray pyrolysis method: structural, optical and magneto-optical properties", *Indian J. Sci. Technol.*, 5(6) (2012).
[23] G. Zheng et al., "Enhanced photocatalytic activity of ZnO thin films deriving from a porous structure", Mater. Lett., 150 (2015) 1-4.

Formation of Inter-Layer Metallic Vertical Links Using Pulsed Laser

Wie Zahng, Xieowan Xei

Department of Electrical and Electronic Engineering, Chengdu University, Chengdu, CHINA

Abstract
In this work, metallic link was formed vertically between two metal layers by using pulsed laser. Finite element analysis is employed to investigate the involved thermal and mechanical behaviors. The energy dependence of the link formation is also qualitatively discussed. Experiments show the link resistance is less than 1.0 Ω at room temperature at accelerated current density of $3x10^6$ A/cm^2. The basic technology is shown to be scalable down to one micron lower metal based on the commercially available laser system.

Keywords: Metallic link; Laser processing; Inter-layer connections; Microelectronics
Received: 18 March 2023; **Revised:** 07 June 2023; **Accepted:** 14 June 2023; **Published:** 1 September 2023

1. Introduction

The principle of link formation employs the contrast of material properties between the metal and the surrounding dielectrics SiO_2/Si_3N_4 [1-3]. Figure (1) schematically illustrates the layout and the cross section from Plane A-A' of a vertical link structure [4]. The IR laser beam passing through the square hole of the upper metal (M2) frame is impinged on the lower metal (M1) line with negligible loss of energy in the covering dielectrics. The laser energy is absorbed on the surface of M1 to be resulting in a sharp metal temperature increase. Due to the extremely low thermal conductivity and light absorbency of the dielectrics, the dielectric temperature is not changed so much. In the meantime, metal expansion fractures the surrounding dielectrics along the stress concentration paths and molten metal fills in the crack [5,6]. At an optimal laser energy and spot size, dielectric cracks can be controlled to initiate from the upper corners of the M1 line and terminate near the inside lower corners of the M2 frame without propagating to the outside of the structure or fracturing the top dielectric passivation.

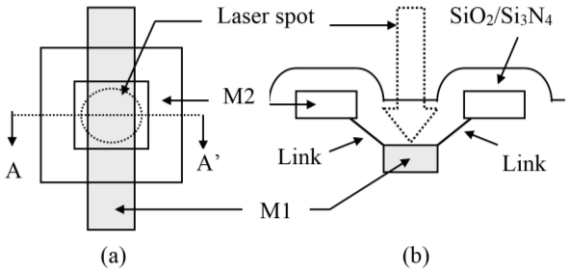

Fig. (1) Schematics of laser-induced vertical metal link, (a) top view and (b) cross section A-A' [2]

2. Experimental Part

Samples were fabricated by a standard commercial two-level metal CMOS process. The metallization consists of a layer of Al-0.5%Cu-1%Si, 550 nm thick for M1 and 750 nm thick for M2. The Al alloy is over-coated and undercoated by 25 nm thick and 50 nm thick TiN films, respectively. The vertical link structure has a 2 μm wide M2 frame with a square hole aligned to the underneath M1 line. Limited by our current laser system, the frame holes used in this study are 6×6 and 4×4 μm, and the M1 linewidths 4 and 3 μm, respectively. The layout was patterned to form series chains in such a way that each chain contains maximum 1320 link cells with probing pads at the 2nd, 24th and 216th link cells to ease resistance measurements. Samples were processed by an XRL 525 IR laser system (1047 nm wavelength and 15 ns

pulse) with specific energies and spot sizes. The details of sample fabrication and laser process can be found in the previous articles [7,8]. The average single-link resistance was evaluated by the total resistance divided by the number of links in a chain (1320). The link electrical resistance depends on laser conditions. For structures with 6×6 μm M2 hole and 4 μm M1 line, which were zapped under a 0.7 μJ laser energy and a 3.0 μm round Full-Width Half Maximum (FWHM) spot size, the link resistance has been observed to be about 0.8Ω. In the measurement, the series resistance was included, so the true value of the average single-link resistance could be smaller than the observed ones.

The voids remaining in the M1 line after metal flows could arouse reliability issues concerning electromigration. The links were stressed at accelerated current density (3MA/cm^2) and temperature (300°C). It is found that the electromigration related lifetime is strongly dependent on laser energy. For the present link structure, the optimal energy value is about 0.7 μJ, as shown in Fig. (2).

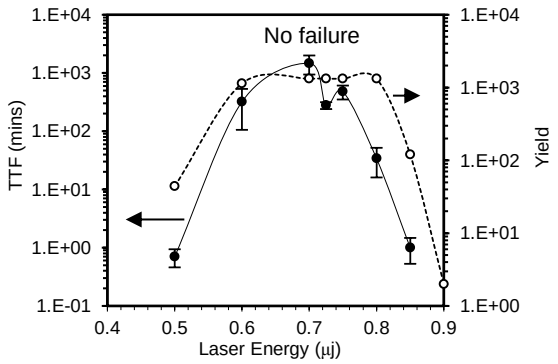

Fig. (2) Link lifetime and yield as functions of laser energy. The lifetime data were obtained at 300°C and 3MA/cm^2

We can also find the same trend for the yield data that is shown in the same figure in comparison with the lifetime curve. For links with a 3 μm M1 line and a 4×4 μm M2 hole, 64680 samples have been successfully processed at 0.6 μJ without failure. It should be pointed out that the link size is scalable based upon the available commercial laser system. The scalability will be discussed in a separate section.

3. Results and Discussion

Finite element analysis (FEA) has been conducted to understand the thermal and mechanical process during the link formation. The simulated link structure consists of a 0.5 μm thick, 2 μm wide lower metal line (M1) and a 0.7 μm thick, 2 μm wide metal frame (M2) with a 3×3 μm square hole. The structure is symmetric about the center, so only a quarter of the structure is modeled. For simplicity, a 2-D model is established assuming plane strain in the cross section along the diameter of the 2.5 μm (FWHM size) round laser spot, which is normal to the M1 line [9]. This assumption is reasonable because of the good thermal conduction of metal and the relatively uniform temperature distribution within a thermal diffusion length. Ordinary thermal boundary conditions include constant temperature (300K) at the bottom and zero heat flux across the left side (center line). Laser radiation on the metal surface is simulated by a Gaussian distributed heat flux. The power density is determined by the following equation [10]:

$$p(x,y,t) = \frac{I(t)}{2\pi\sigma^2}\exp\left(-\frac{x^2+y^2}{2\sigma^2}\right) \qquad (1)$$

$$\int_0^{\infty}\int_{-\infty}^{\infty}\int_{-\infty}^{\infty} p(x,y,t)\,dx\,dy\,dt = E$$

where $p\,(x, y, t)$ is the laser power density at (x , y) and time t, E the total laser energy, $I(t)$ the power density in the center of the laser spot at time t, which is modeled according to the measured power output as shown in Fig. (3), σ is the standard deviation of the Gaussian distribution. For a 2.5 μm FWHM spot, σ=1.06 μm

In this 2-D simulation, the line power density is emulated by a 1-D normal distribution. A critical stress about 300 MPa is used to judge the SiO_2 fracture. The material properties are taken from previous works [11-13]. It should be pointed out that the initial residual stress in the metal was

also calculated assuming zero stress at 200°C, and the thermal and mechanical properties of pure aluminum are employed .

At 0.6 μJ, the temperature and stress change with time for SiO_2 near the upper corner of M1 is shown in Fig. (4). The SiO_2 crack is initiated from the upper corner when the principal normal max stress is about 300 MPa and the corresponding SiO_2 temperature about 850 K. In the meantime, Al temperature is close to the melting point. The dielectric crack propagates approximately at the velocity of sound toward the upper frame (M2) with an angle of about 40-45 degree. Monitoring the stress evolution also allows us to understand the crack propagation [14]. As can be seen in the stress curve in Fig. (4), the first peak indicates the crack initiation while the second indicates the crack reaching the upper frame. Stress accumulation and release can be seen during the crack propagation.

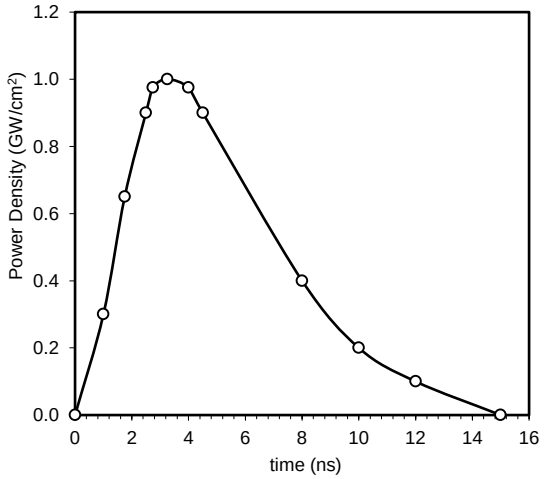

Fig. (3) The variation of laser power density with pulse duration used in this work

Simulations at different laser energies (0.2μJ, 0.4μJ and 0.6μJ) were also conducted. Figure (5) shows the link trajectory at different energies. At 0.2 μJ, the cracking stopped in the middle between M1 and M2, and failed to form a valid electrical connection, while at 0.6 μJ, the energy is too high so that the crack continues to propagate along the bottom plane of M2 after it reaches the frame. Excessive M1 metal flow results in large voids in the lower metal that increases electromigration risk; in the meantime, the undesired crack outside the link frame can destroy the completeness of the top passivation. Therefore, at a range around the optimal energy (0.4 μJ) can the process ensure a solid link and prevent reliability problems. It is worthy to note that there is an energy shift between experiments and simulation, since the reflectivity of metal surface is ignored [15,16].

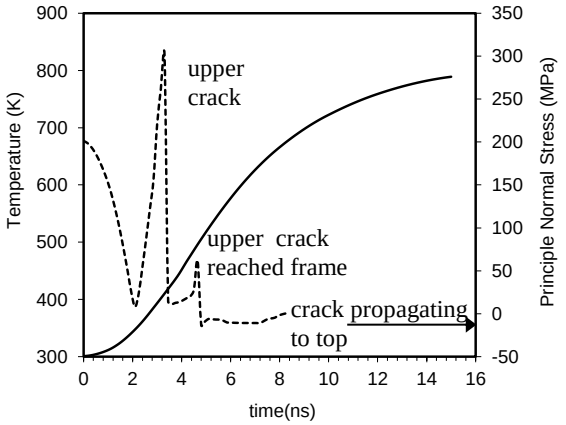

Fig. (4) Upper corner SiO_2 temperature (solid line) and principle normal maximum stress (dash line) evolution as a function of time at 0.6 μJ

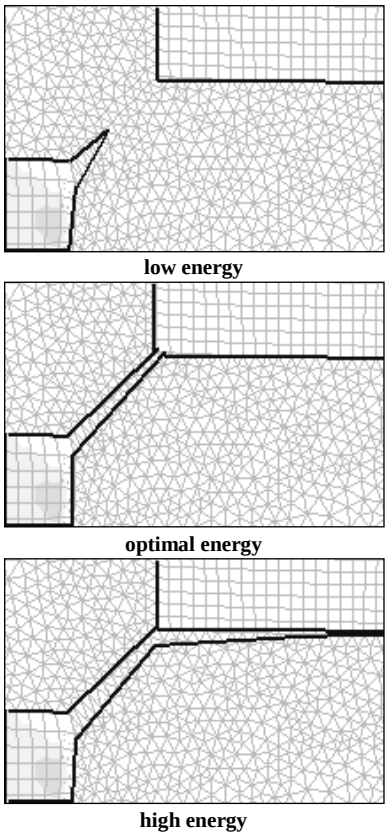

Fig. (5) Laser energy dependence of crack length. The optimal energy suggested by the current simulation is about 0.6μJ

4. Conclusion

According to the results obtained from this work, the link presents low resistance (0.8Ω), high yield and reliability. Finite element analysis shows an optimal laser energy that is relatively consistent with the experimental results. A simple link sheet model is proposed to estimate the scalability. Results indicate the lower metal width can be scalable to 1 μm.

References

[1] A. Ascari et al., "Long Pulse Laser Micro Welding of Commercially Pure Titanium Thin Sheets", *Proced. Eng.*, 184 (2017) 274-283.

[2] A. Giesriegl et al., "Laser diagnostics and processing of historical and artificial copper patina", *J. Cultur. Herit.*, 62 (2023) 45-53.

[3] O.A. Hamadi and K.S. Khashan, "Effect of Preheating on the Parameters of Laser Keyhole Welding Process: Analytical Study", *Iraqi J. Laser, Part A*, 5(5) (2006) 11-17.

[4] A. Otto, H. Koch and R.G. Vazquez, "Multiphysical Simulation of Laser Material Processing", *Phys. Proced.*, 39 (2012) 843-852.

[5] D. Semenok, "LCLD Laser Processing Technology for Microelectronics Printed- circuit Boards of New Generation", *Proced. Technol.*, 12 (2014) 277-282.

[6] O.A. Hamadi, "Employment some parameters to enhance laser drilling of aluminium", *J. Sci. Technol., Sultan Qaboos Univ.*, 10 (2005) 93-100.

[7] D.W. Müller et al., "Multi-pulse agglomeration effects on ultrashort pulsed direct laser interference patterning of Cu", *Appl. Surf. Sci.*, 611(Part A) (2023) 155538.

[8] O.A. Hammadi, "Using Third-Harmonic Radiation of Nd:YAG Laser to Fabricate High-Quality Microchannels for Biomedical Applications", *Optik*, 208 (2020) 164147.

[9] I. Geoffray, R. Bourdenet and M. Theobald, "Laser Micro-welding Applied to Target Manufacturing", *Phys. Proced.*, 12(Part B) (2011) 363-369.

[10] K. Plat et al., "Laser Processing of Thin Glass Printed Circuit Boards with a Picosecond Laser at 515nm Wavelength", *Phys. Proced.*, 56 (2014) 983-990.

[11] O.A. Hamadi, "HAZ extent analysis in fiber-reinforced plastic grooving by laser", *Iraqi J. Appl. Phys.*, 1(1) (2005) 1-7.

[12] R. Delmdahl, R. Pätzel and J. Brune, "Large-Area Laser-Lift-Off Processing in Microelectronics", *Phys. Proced.*, 41 (2013) 241-248.

[13] S. Akinlabi and E. Akinlabi, "Laser Beam Forming: A Sustainable Manufacturing Process", *Proced. Manufact.*, 21 (2018) 76-83.

[14] O.A. Hammadi, "Fabrication of High-Quality Microchannels for Biomedical Applications Using Third-Harmonic Radiation of Nd:YAG Laser", *J. Laser Sci. Eng.*, 10(2) (2018) 61-64.

[15] X.-L. Cao et al., "Effect of process parameters on microstructure and properties of laser welded joints of aluminum/steel with Ni/Cu interlayer", *Trans. Nonferrous Metals Soc. China*, 31(8) (20210 2277-2286.

[16] O.A. Hamadi and K.S. Khashan, "Modeling of the Preheating Effect on Keyhole Laser Welding Efficiency", *Iraqi J. Appl. Phys. Lett.*, 1(1) (2008) 10-15.

Raman Cell for Measurement of Temporal Coherence Length Using UV Diode Laser

Mahdi S. Edan

Al-Rasheed University College, Baghdad, IRAQ

Abstract
In this work, the temporal coherence length was measured as a function of hydrogen gas pressure inside a Raman cell using pulsed diode laser with 375nm wavelength. The results showed that the temporal coherence length is rapidly increasing with increasing the input energy inside the Raman cell before this increase got slow at a certain value of input energy as the nonlinear effects of the gaseous medium appeared. This principle of measurement can be employed to study the gaseous media accurately as the probing tool is simply a monochromatic coherent light beam.

Keywords: Raman cell; Gaseous absorption; UV laser; Nonlinear optics
Received: 29 April 2023; **Revised:** 27 May 2023; **Accepted:** 05 June 2023; **Published:** 1 July 2023

1. Introduction

Temporal coherence expresses the ability to control the amplitude and phase of the coherent electromagnetic wave in time [1]. It is a feature related to the monochromaticity of such wave as the coherence time is extended when the possibility of narrowing the spectral linewidth gets wider [2]. The temporal coherence length (L_c), i.e., the distance traversed by the wave within coherence time, is the product of coherence time (Δt) by the velocity (c) of the electromagnetic wave (light) in vacuum as [1]:

$$L_c = c.\Delta t \quad (1)$$

Laser sources with controlled temporal coherence properties have a great importance in spectroscopic analysis as they can be used for efficient and simultaneous excitation of energetic systems in order to make use of their fluorescence [4-6]. This exceptional advantage is very important in biological diagnosis based on the spectroscopic characteristics [7]. Also, the light sources of high directionality (such as lasers) can be used in optical microscopy in order to produce the minimum optical distortion in the sample under study [8]. Accordingly, the coherent light beam can be successfully employed for this purpose as their temporal coherence properties are controlled to minimize the optical distortion mentioned before [9,10]. The most appropriate laser sources for this purpose are UV diode lasers. However, the limited tuning range of the output of these lasers may restrict their use in microscopic investigations based totally on the fluorescence [11]. Therefore, some effective techniques are used to produce a shift in the wavelength of the laser source and one of these techniques is stimulated Raman scattering (SRS) [12]. In this technique, a simultaneous generation of the spectral line (or multiple spectral lines) can be achieved from the vacuum UV (VUV) region to far IR (FIR) region [13-16].

In conventional spontaneous Raman scattering, an incident pumping photon with frequency of ω_p is exciting the molecule from the ground state to a higher excited state [17]. When the molecule relaxes to the first excited state, it emits a shifted-wavelength photon with frequency of ω_s, which is lower than ω_p ($\omega_s < \omega_p$). This mode of scattering is known as Stokes mode. If the molecule is already exists at an excited state and absorbs the energy of the incident photon and relaxes to the ground state, then a wavelength-shifted photon will also be

emitted but with a frequency of ω_{as}, which is higher than ω_p ($\omega_{as} > \omega_p$). This mode is known as anti-Stokes mode [1]. The Raman shift frequency (ω_R) is given by [18]:

$$\omega_R = \frac{2\pi E_1}{h} \qquad (2)$$

where E_1 is the energy of the first excited state and h is Planck's constant

The Raman scattering in both modes (Stokes and anti-Stokes) is a potential characteristic of many active media and hydrogen (H_2) gaseous medium can produce the highest Raman shift frequency (ω_R=4155.2cm^{-1}) [19,20].

The SRS is a result of the interaction between the high-intensity pumping beam and the medium exhibiting Raman effect. This interaction is described by the product of a pair of identical photons in Stokes mode during the interaction of pumping photon with the active medium in presence of one photon in Stokes mode. Therefore, the SRS is coherent and higher in intensity when compared to the conventional Raman scattering, which is incoherent and lower in intensity [21,22].

If the intensity of the first Stokes photon of ω_{s1} frequency is sufficiently high, then another effect of the SRS is induced to produce a pair of second-order Stokes photons with frequency of ω_{s2}. Consequently, the SRS can be employed to produce Stokes photons with higher orders and frequencies (ω_{s3}, ω_{s4} … etc.) [23].

In this work, the temporal coherence length was measured for the output signal from a Raman cell containing hydrogen gas. As the gas pressure inside this cell is varied, this medium exhibits Raman effect when irradiated with UV laser pulses. The value of temporal coherence length was determined by performing the inverse Fourier transformation (IFT) on the spectrum of the output signal from Raman cell.

2. Experimental Part

Figure (1) shows the experimental setup used in this work. A USHIO UV diode laser with wavelength of 375nm, maximum pulse energy of 1mJ, pulse duration of 1ms and Gaussian mode (TEM_{00}) was used as the coherent light source. The laser pulse energy (input energy) could be controlled by controlling the operation power. The pulse energy was measured using a Molectron-J25HR detector.

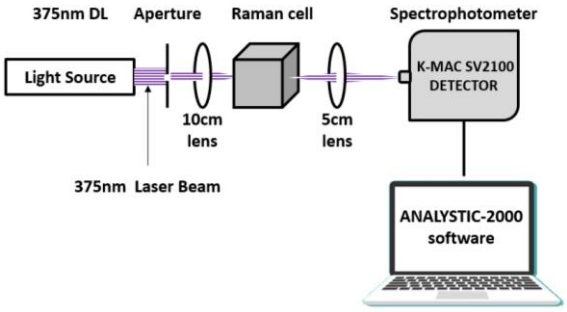

Fig. (1) Experimental setup used in this work

An aperture and 10cm focal lens were used to confine and focus the laser beam on the Raman cell, which was made of a 10cm long stainless steel cylinder, whose both ends were closed with a glass windows. These windows contain two inlets to suck the air from the cell and pump the gas into it.

Three different gases (hydrogen, nitrogen and ammonia) were examined to fill the cell and the hydrogen was selected to be the active medium. The maximum gas pressure inside the cell was 35 bar. This Raman cell was mounted with respect to the spectrophotometer in order the output signal from the cell is incident on the detector unit of the spectrophotometer using a 5cm focal lens. A SpectraAcademy SV-2100 spectrophotometer was used. This instrument operates in the spectral range 196-962nm with a resolution of ±0.2nm and can be connected to a PC to transfer and process the experimental data. The obtained spectra were processed by ANALYSTIC-2000 software to perform the IFT and hence determine the temporal coherence length.

3. Results and Discussion

Figure (2) shows the variation of temporal coherence length (L_c) with hydrogen gas pressure inside Raman cell for input laser pulse of 1mJ. It is noted that the value of L_c decreases with the initial increase in gas pressure to a point after which the

increase got rapid. Then, a saturation point is reached as the value of L_c became constant with further increase in gas pressure. The increase of L_c determines a threshold value of gas pressure at which the SRS starts to appear in both modes (Stokes and anti-Stokes) until a certain pressure at which the nonlinear effects dominates the effect of Raman scattering and then damp it while the value of L_c is kept constant to represent a saturation state over the range of gas pressures used. Consequently, there is a limited distance that the coherent beam can traverse while its temporal coherence properties are kept with varying density of the medium causing this effect.

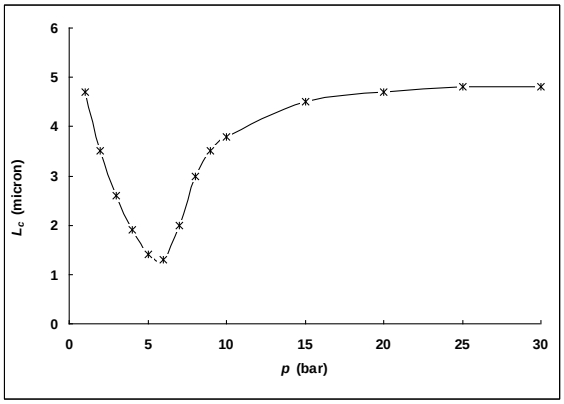

Fig. (2) Variation of temporal coherence length with the gas pressure inside Raman cell

Figure (3) shows the variation of temporal coherence length (L_c) with the input energy (laser pulse energy) at three different values of hydrogen gas pressures inside Raman cell (2, 6.5 and 20 bar). It can be seen that the variation of L_c with input energy is different according to the value of gas pressure inside the cell. It rapidly decreases with input energy at gas pressure of 2 bar, which lower than the threshold value required for the SRS to appear. The variation of L_c is slow when the gas pressure inside the cell is increased to 6.5 bar, which approximately represents a threshold or critical value between the ordinary scattering effect of laser beam passing through the gas medium and the initiation of the SRS. At higher values of gas pressure inside the cell (20 bar), the variation of L_c is apparently rapid with increasing input laser pulse energy. However, a saturation point is reached and the further increase in the input laser pulse energy does not lead to keep the temporal coherence properties for longer distance than what was obtained before.

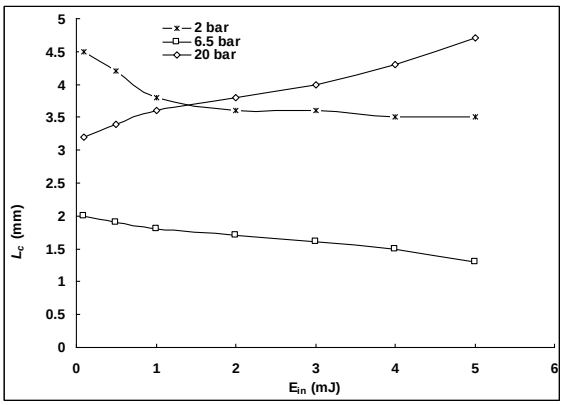

Fig. (3) Variation of temporal coherence length (L_c) with the input laser pulse energy (E_{in}) at three different values of gas pressure inside Raman cell

The output spectrum of the Raman cell was recorded in the spectral range of 200-500nm in order to recognize the spectral lines generated in the Raman cell as a result of Stokes and anti-Stokes scattering, as shown in Fig. (4). Two Stokes lines can be observed at 394 and 477nm and two anti-Stokes lines can be observed at 293 and 259nm as a response to the incident laser pulse due to SRS effect.

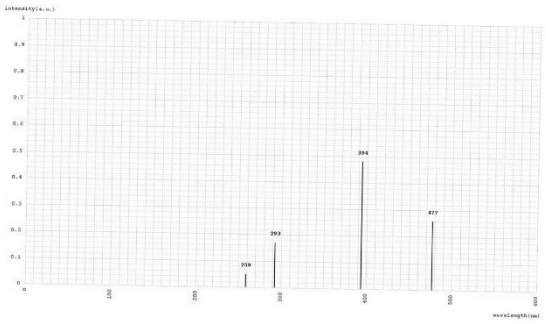

Fig. (4) Spectral peaks generated in the Raman cell as a result of the SRS

4. Conclusion

In concluding remarks, the temporal coherence length of a coherent electromagnetic wave traversing through a medium showing Raman scattering effect is reasonably dependent on the density of this medium (gas pressure) as well as on the

wave energy. Also, there is a threshold for the density (gas pressure) as the temporal coherence length decreases with increasing gas pressure before reaching this threshold due to the spontaneous scattering effects, which limit the ability of the coherent electromagnetic wave to keep its temporal coherence properties. The effect of stimulated Raman scattering starts to appear beyond this threshold as the temporal coherence length increases rapidly to reach a constant value and a saturation point. The further increase in the density of the medium (gas pressure) beyond the saturation point causes the nonlinear effects to appear within this medium.

References

[1] C. Banwell, **"Fundamentals of Molecular Spectroscopy"**, 3rd ed., McGraw-Hill Book Co. (London, 1983).

[2] A.I. Vodchits et al., "Efficient multi-frequency generation of ultrashort light pulses using stimulated Raman scattering and optical parametric amplification", *Opt. Commun.*, 260(1) (2006) 307-310.

[3] Z. Wu et al., "Efficient dual-wavelength stimulated Raman scattering derived from CH_3 and OH stretching vibrations in ethanol–water blend", *Opt. Lasers Eng.*, 126 (2020) 105868.

[4] C. Wang et al., "Cascaded amplification via three-beam double stimulated Raman scattering in benzene", *J. Mol. Liq.*, 368(Pt A) (2022) 120667.

[5] Z. Dou et al., "Pulse compression and spectral broadening of stimulated Raman scattering in water via cascading amplification", *Opt. Commun.*, 501 (2021) 127393.

[6] Y. Wang et al., "Resonance enhancement stimulated Raman scattering of O–H stretching vibration in water molecule", *J. Mol. Liq.*, 324 (2021) 114722.

[7] D. Bi et al., "Stimulated low-frequency Raman scattering of light: An effective way of laser Q-switching", *Opt. Laser Technol.*, 156 (2022) 108559.

[8] F.A. Bajafar and R.M. Altuwirqi, "Numerical modeling of stimulated Raman scattering with selective amplification", *J. Mol. Spectro.*, 318 (2015) 64-69.

[9] M. Xu et al., "High efficiency ethane Raman laser pumped by 532 nm laser", *Res. Opt.*, 12 (2023) 100436.

[10] Y. Wang et al., "Exploring hydrogen bonds network behavior of ethanol-water systems on stimulated Raman scattering", *J. Mol. Liq.*, 295 (2019) 111705.

[11] T.Y. Chen et al., "Time-domain modelling and thermometry of the CH_4 ν1 Q-branch using hybrid femtosecond/picosecond coherent anti-Stokes Raman scattering", *Combus. Flame*, 224 (2021) 183-195.

[12] A.I. Vodchits et al., "Influence of gas circulation on stimulated Raman scattering and amplification of ultrashort laser pulses in methane", *Opt. Commun.*, 281(11) (2008) 3190-3195.

[13] Y. Jia et al., "Near IR Raman laser beams generated by 1064 nm pumped Stimulated Raman Scattering (SRS) of pressurized nitrogen", *Opt. Commun.*, 529 (2023) 129019.

[14] S. Marchetti et al., "Analysis of the 2nd Stokes wave generation through stimulated Raman scattering in hydrogen gas under four-wave mixing conditions", *Opt. Commun.*, 282(14) (2009) 2954-2959.

[15] Y. Gao et al., "Stimulated Raman scattering investigation of isotopic substitution H_2O/D_2O system", *J. Mol. Liq.*, 297 (2020) 111923.

[16] P.G. Zverev, T.T. Basiev and A.M. Prokhorov, "Stimulated Raman scattering of laser radiation in Raman crystals", *Opt. Mater.*, 11(4) (1999) 335-352.

[17] X.F. Wang, R. Fedosejevs and G.D. Tsakiris, "Observation of Raman scattering and hard X-rays in short pulse laser interaction with high density hydrogen gas", *Opt. Commun.*, 146(1-6) (1998) 363-370.

[18] N.J. Everall et al., "Threshold measurements of stimulated Raman scattering in gases using picosecond KrF laser pulses", *Opt. Commun.*, 64(4) (1987) 393-397.

[19] E. Berik et al., "Stimulated Raman scattering of dye laser radiation in hydrogen. Improvement of spectral purity", *Opt. Commun.*, 56(4) (1985) 283-287.

[20] X. Liu et al., "Resonance enhanced cascaded stimulated Raman and Coherent Anti-Stokes Raman scattering of symmetric and antisymmetric O-D vibrations", *Opt. Commun.*, 509 (2022) 127861.

[21] T. Zheng et al., "The investigation of stimulated Raman scattering in gases under di-harmonic pumping", *Opt. Commun.*, 516 (2022) 128246.

[22] S. Mamani, H.E. Ahmar and R.R. Alfano, "Orbital and spin angular momentum Raman scattering of methanol, benzene, hexane, and carbon tetrachloride liquids", *Optik*, 267 (2022) 169727.

[23] C. Wang et al., "Shock compression-induced enhancement of stimulated Raman scattering in heavy water", *Opt. Commun.*, 501 (2021) 127394.

IRAQI JOURNAL OF APPLIED PHYSICS LETTERS
EDITORIAL BOARD

COPYRIGHT RELEASE FORM

IRAQI JOURNAL OF
APPLIED PHYSICS LETTERS (IJAPLett)

We, the undersigned, the author/authors of the article titled

……
……
……
……
……
……
……

that is submitted to the Iraqi Journal of Applied Physics Letters (IJAPLett) for publication, declare that we have neither taken part or full text from any published work by others, nor presented or published it elsewhere in any other journal. We also declare transferring copyrights and conduct of this article to the Iraqi Journal of Applied Physics Letters (IJAPLett) after accepting it for publication.

The authors will keep the following rights:

1. Possession of the article such as patent rights.
2. Free of charge use of the article or part of it in any future work by the authors such as books and lecture notes after informing IJAP editorial board.
3. Republishing the article for any personal purposes of the authors after taking journal permission.

To be signed by all authors:

Signature:……..date: ……
Printed name: ……

Signature:……..date: ……
Printed name: ……

Signature:……..date: ……
Printed name: ……

Correspondence author:……...
……
Address:……
……
Telephone:……..……..email: ……

Note: Complete and sign this form and mail it to the below address with your finally revised manuscript

The Iraqi Journal of Applied Physics Letters
P. O. Box 88052, Baghdad 12631, IRAQ
www.iraqiphysicsjournal.com
Email: editor@iraqiphysicsjournal.com
Email: editor_ijap@yahoo.co.uk
Email: ijaplett.editor@gmail.com

IRAQI JOURNAL OF APPLIED PHYSICS LETTERS
Volume (6) Issue (3) July-September 2023

CONTENTS